UBIAT

UBI AERONAUTICS TEAM

FROM COVILHÃ
TO THE SKIES



AIR CARGO CHALLENGE 2026

TECHNICAL REPORT - TEAM #13

DESIGN • INNOVATE • DELIVER

Contents

1 Introduction **3**

1.1 UBI Aeronautics Team . . . 3

1.2 Project Management . . . 3

1.3 Financial Management . . . 5

2 Aerodynamic Design **6**

2.1 Initial Design . . . 6

2.2 Airfoil Selection . . . 7

2.3 High-Lift Devices . . . 8

2.4 Fuselage . . . 9

2.5 Wing Selection . . . 11

2.6 Wing Optimization . . . 12

2.7 Design Results and Payload . . . 13

2.8 Stability and Control . . . 15

3 Payload Prediction **16**

4 Structural Design **16**

4.1 Wing Structure . . . 17

4.2 Nose, Central Fuselage and Payload . . . 18

4.3 Aft Fuselage and Empennage . . . 20

4.4 Landing Gear . . . 22

5 Propulsion System **24**

5.1 ESC Selection . . . 24

5.2 Propeller Selection . . . 24

5.3 Main Battery Selection . . . 25

5.4 Motor Fine-tuning . . . 25

6 Electronic Components **26**

6.1 Servos Selection . . . 26

6.2 Secondary Battery Selection . . . 26

7 Circuits Assembly **27**

7.1 Mass Prediction Validation . . . 27

8 Manufacturing **27**

8.1 Wing and V-tail . . . 28

8.2 Fuselage . . . 28

8.3 Fowler Flap . . . 29

8.4 Landing Gear . . . 29

9 Conclusion and Outlook **30**

1 Introduction

1.1 UBI Aeronautics Team

UBIAT is a team comprised of students from Universidade da Beira Interior, Portugal, which follows on from the Aero@UBI team. Since 2003, the team has been participating in UAV design and building competitions, such as Air Cargo Challenge (ACC), Design/Build/Fly (DBF), and AeroCup, as presented in Table 1.

Table 1: University's participation log.

Competition	Year	Location	Organizer	Team Placement
ACC	2003	Ota, Portugal	APAE	1st Place
ACC	2005	Lisbon, Portugal	APAE	3rd and 6th Place
ACC	2007	Lisbon, Portugal	APAE & EUROAVIA	1st Place
ACC	2009	Covilhã, Portugal	AS Covilhã	Organizer
ACC	2011	Stuttgart, Germany	AS Stuttgart & APAE	1st Place
ACC	2013	Ota, Portugal	AS Covilhã	Organizer
ACC	2015	Stuttgart, Germany	AS Stuttgart	5th Place
ACC	2017	Zagreb, Croatia	AS Zagreb	20th and 23rd Place
ACC	2019	Stuttgart, Germany	AS Stuttgart	5th Place
ACC	2022	Munich, Germany	AS Munich	13th Place
ACC	2024	Aachen, Germany	AS Aachen & ADDI	3rd Place
DBF	2025	Arizona, USA	AIAA	28th Place
AeroCup	2025	Lisbon, Portugal	ACC alumni	1st Place

1.2 Project Management

UBIAT is composed of a team leader, 6 coordinators, 21 members, the professor in charge, and 9 advisors – one university professor, the long-standing pilot, and 7 alumni advisors. While the team operates under student leadership, the advisors provide guidance and share their scientific and technical expertise. It is important to note that 9 members of the team are master's students, while 19 are bachelor's students.
The diagram presented in Figure 1 illustrates how the team is organized, the professor in charge, faculty advisor, pilot and coordinator's names.

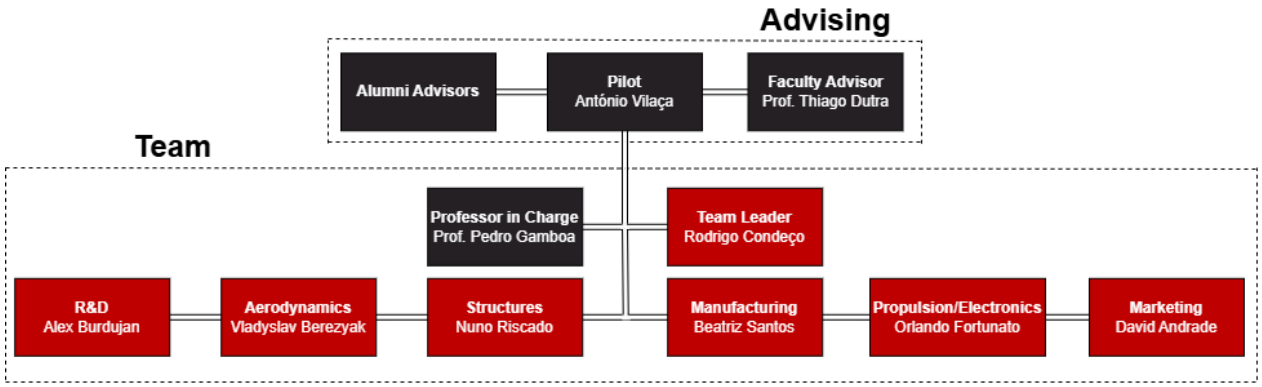


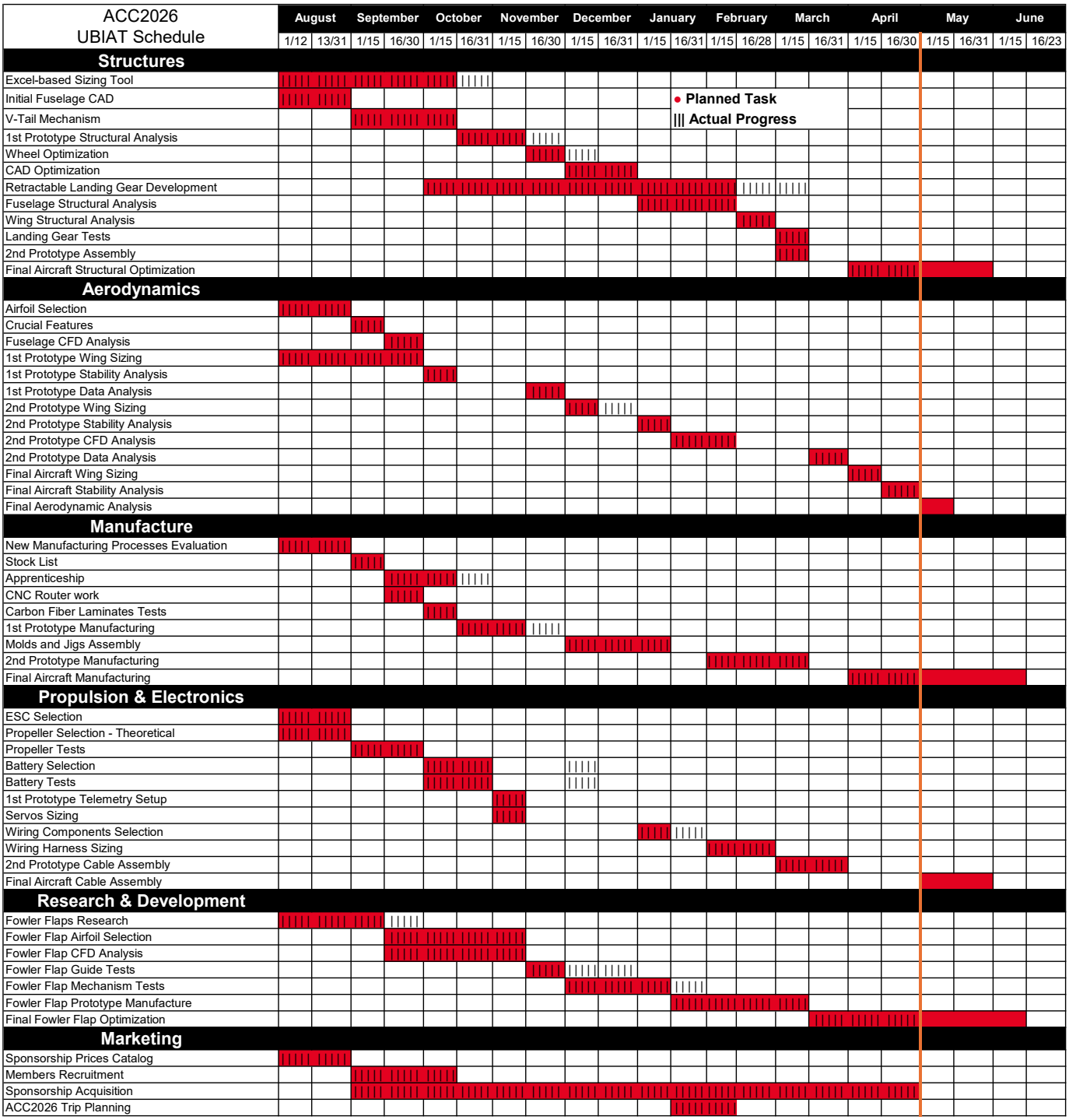
Figure 1: Team distribution.

There are several technical sections within the team. The Aerodynamics section is responsible for the analysis and optimization of the aircraft's aerodynamic performance, including airfoil selection, drag estimation, stability and control, often using CFD and experimental data. The Structures section designs and analyzes the structural components of the aircraft ensuring structural integrity and weight efficiency, through CAD modeling and simulations. The Propulsion and Electronics section is responsible for the selection of the propulsion system components, including propeller, batteries, wiring, servos, performance optimization, and systems integration. The Research and Development section focuses on innovation and testing of new mechanisms and

concepts, validating solutions through prototyping and iterative design. The Manufacturing section focuses on defining and applying manufacturing techniques and on the assembly processes required to achieve the final aircraft, including mold fabrication and machining. Additionally, there is a non-technical section, Marketing, which manages sponsorships, communication, and public relations, while documenting the team's work and promoting the project externally.

At the start of August 2025, the team started planning the timeline for the ACC2026, as presented in Table 2.

Table 2: UBIAT timeline for ACC2026.



The main decisions for the project are made during the weekly coordinators' meetings, with the team leader and coordinators in attendance. Additionally, weekly section meetings are held, where all work is distributed,

analyzed, and members are updated on the decisions made during the coordinators' meetings.
Finally, monthly general meetings are conducted, during which each coordinator presents the work accomplished by their respective section throughout the month, updating every other section with their progress.

1.3 Financial Management

The financial management of UBIAT ensures an efficient and transparent use of resources for the ACC2026 competition. The team started this academic year with an initial surplus of € 2,098.76 carried over from the previous academic year, during which it participated in the DBF2025 and AeroCup 2025 competitions, providing a solid foundation for the early stages of the project.
This budget is complemented by sponsorships, allowing the team to meet the technical and logistical demands of the competition. The following sections present an overview of the team's sponsors and the distribution of expenses.

1.3.1 Sponsors

UBIAT acknowledges the fundamental support of its sponsors, whose contributions make the participation in ACC2026 possible. The sponsorship structure includes both financial support and tailored contributions such as materials, manufacturing services, and technical assistance. Each sponsor is presented according to their type of sponsorship in Tables 3 and 4.

Table 3: UBIAT monetary sponsors.

Entity name	Sponsorship tier	Contribution (taxes included)
TEKEVER	Main	€ 6,118.00
Orion Technik	Premium	€ 2,500.00
GO WALK Engenharia	Premium	€ 1,353.00
ANAC	Premium	€ 1,353.00
Universidade da Beira Interior	Premium	€ 1,000.00
NAV Portugal	Gold	€ 861.00
AEROUBI & AS Covilhã	Gold	€ 500.00
COFICAB	Silver	€ 430.50
Dassault Business	Silver	€ 430.50
Himá Oriental Taste	Silver	€ 430.50
Connect Robotics	Bronze	€ 184.50
Águas da Covilhã	Bronze	€ 184.50
	Total	€ 15,345.50

Table 4: UBIAT non-monetary sponsors.

Entity name	Sponsorship tier	Contribution
EDM Tech	Premium	Acquisition of a laser cutting machine
CEiiA	Premium	Manufacturing of the wing molds
Eliot	Premium	Manufacturing of the wing molds
UBI | Faculdade de Engenharia	Premium	Competition registration fees
Produtos Sodacasa	Gold	Composite manufacturing materials
Gomill	Silver	CNC machining of parts
Dassault Systémes	Partner	SOLIDWORKS premium licenses
ESSS + ANSYS®	Partner	ANSYS® premium licenses
Redbull Portugal	Partner	Donation of Redbull cans
CN Models	Partner	50% discount
R&G Composites	Partner	20 % discount
Easy Composites	Partner	10% discount

1.3.2 Expenses

The team's expenses are carefully planned and monitored to ensure the efficient use of available resources. Since the competition aircraft is currently being manufactured, Table 5 presents a breakdown of estimated expenses.

Table 5: Estimated expenses.

Category	Description	Estimated cost
Materials & manufacturing	Composite materials, wood, adhesives, 3D printing, machining	€ 4,500.00
Electronics & systems	Servos, batteries, wiring, control systems	€ 1,700.00
Transportation & logistics	Travel, accommodation, aircraft transport	€ 1,400.00
Marketing & promotion	Team branding, promotional materials, events	€ 600.00
Miscellaneous costs	Tools, unexpected expenses, contingency	€ 1,400.00
	Total	€ 9,600.00

All expenditures are tracked throughout the project to ensure compliance with the allocated budget. Regular financial reviews are conducted to maintain cost control and allow adjustments when necessary. It is also important to highlight that the overall expenses include the design, development, and production of two prototypes, as well as the final competition aircraft, all developed by the team. These prototypes constitute a significant share of the project's total costs, as they require substantial investment in materials, manufacturing processes, testing, and iterative refinement, all of which are essential to meeting the project's technical objectives.

2 Aerodynamic Design

2.1 Initial Design

The conceptual design was driven by the observation that the ACC2026 mission rewards the best compromise between take-off performance, payload capability and maximum speed during the distance segment [1]. Since loading and unloading time also contributes to the final score, the aircraft had to be conceived not only for aerodynamic efficiency, but also for operational simplicity.

The primary design choice concerned payload integration. Several can arrangements were studied, and the selected solution was based on two parallel rows, allowing efficient packing while keeping the fuselage cross-section compact and minimizing overall drag [13]. This result in a long payload bay with a slender external shape.

A low-wing configuration was selected as the most favorable solution. Such arrangement leaves the upper side of the fuselage unobstructed, improving loading and unloading, while also taking advantage of ground effect during take-off. In addition, it allows the main retractable landing gear to be integrated into the wing, reducing its length, structural mass and parasite drag. A taildragger layout was adopted because of its simplicity and lower drag [13].

Other concepts were also examined and discarded during this stage. The use of two motors was considered early in the project, but it was eventually rejected due to the increase in structural mass, additional ESCs and cabling, stricter alignment requirements, and the limited current margin available under the total $30\,\mathrm{A}$ limit [1]. The resulting concept was a single-motor, low-wing aircraft with a semi-elliptical wing, a Fowler flap on the central wing panel, which improves take-off and initial climb performance while preserving a clean outer wing for the distance segment, an all-moving V-tail, and a retractable landing gear. This configuration was considered optimal for combining aerodynamic efficiency, payload integration and short take-off capability.

2.2 Airfoil Selection

An initial airfoil selection process was conducted using an iterative, merit-based screening methodology designed to balance the conflicting aerodynamic requirements of the ACC2026 mission [1]. Since the aircraft must simultaneously achieve high cruise speed, strong climb capability, and elevated payload capacity, the selection criteria prioritized aerodynamic metrics directly linked to these mission phases. A low drag coefficient ($C_{d\,\text{min}}$) at cruise was essential to maximize flight speed, while a high maximum lift coefficient ($C_{l\,\text{max}}$) and strong climb efficiency($C_l^{3/2}/C_d$) were required to support take-off performance and payload capability.
The first stage of the airfoil selection process was automated using a *Python*-based screening workflow designed to process a large database of low-Reynolds-number airfoils [2]. The script automatically executed multiple *XFOIL* [3] analyses for each candidate profile under the Reynolds conditions representative of take-off, climb and cruise. From the generated polars, the code extracted the main aerodynamic indicators used in the screening process, namely the maximum lift coefficient, minimum drag coefficient, maximum aerodynamic efficiency $(C_l/C_d)_{\text{max}}$, climb efficiency, and the low-speed take-off efficiency $(C_l/C_d)_{TO}$. These parameters were normalized with respect to the best-performing airfoil in each category and combined through the merit function shown in Equation 1, allowing an objective ranking of all candidate airfoils.

$$f_i = 0.31\frac{C_{d,\text{min}}}{C_{d,i}} + 0.28\frac{(C_l/C_d)_i}{(C_l/C_d)_{\text{max}}} + 0.20\frac{C_{l,\text{max},i}}{C_{l,\text{max}}} + 0.06\frac{\left(C_l^{3/2}/C_d\right)_i}{\left(C_l^{3/2}/C_d\right)_{\text{max}}} + 0.15\frac{(C_l/C_d)_{TO,i}}{(C_l/C_d)_{TO,\text{max}}} \tag{1}$$

The automated workflow then returned the ten highest-scoring airfoils, which were subsequently evaluated in an *Excel*-based [4] wing sizing and aircraft performance assessment methodology described in the following section.
The aerodynamic characteristics of each candidate airfoil were obtained through Type 1 and Type 2 viscous analyses in *XFLR5* [5], performed for several Reynolds numbers and $Re\sqrt{C_l}$ conditions. The main purpose of these analyses was to generate and extrapolate airfoil polars that could later be used in the *Excel*-based sizing and performance assessment [4]. Reynolds numbers between $200\,000$ and $800\,000$ were considered, while Type 2 analyses were additionally performed for values between $220\,000$ and $380\,000$. From these polars, the main aerodynamic characteristics of each airfoil were extracted and then used in the iterative merit-based selection process.
The final automated ranking identified SD7043, E64, and BE50 as the three best-performing candidates, with SD7043 obtaining the highest score. Upon identifying the SD7043 airfoil as the leading candidate, the team performed an inverse design optimization in *XFLR5* [5] to further improve its aerodynamic characteristics. This process was fully iterative, and both the merit function weights and the resulting ranking evolved multiple times throughout the design cycle as the aircraft configuration matured.
The modified airfoil developed during the design process was designated by the team as the “Super” airfoil. The aerodynamic characteristics of the optimized “Super” airfoil are presented in Figures 2 and 3, including the aerodynamic efficiency (C_l/C_d) as a function of lift coefficient and the pitching moment coefficient (C_m–C_l), as well as the lift and drag polars (C_l–α, C_d–α). These results are used to assess the aerodynamic performance and stability behavior across the operating range.

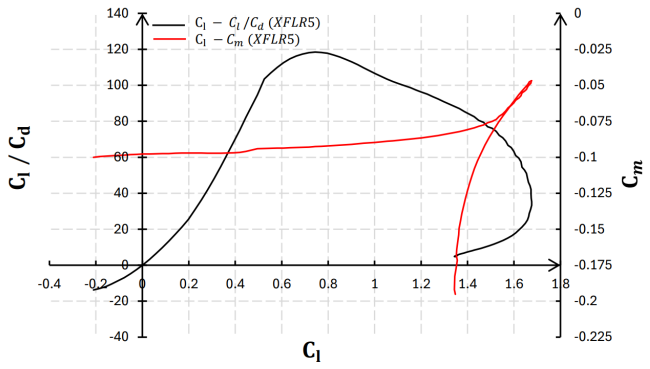


Figure 2: “Super” (C_l/C_d–C_l and C_m–C_l) polars.

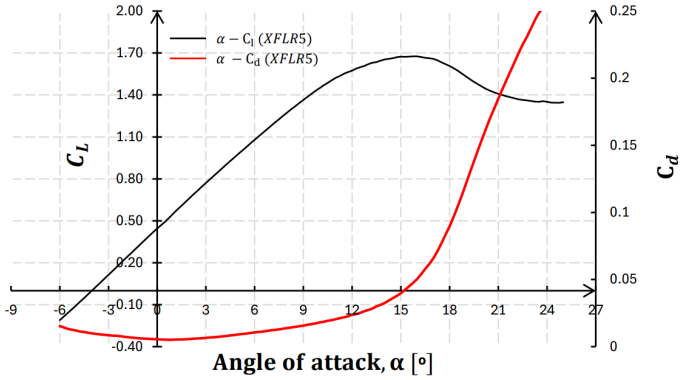


Figure 3: “Super” (C_l–α, C_d–α) polars.

2.3 High-Lift Devices

A flap system was introduced to improve the low-speed aerodynamic performance of the aircraft without compromising the clean-wing condition required during the distance segment. Since the ACC2026 mission rewards payload capability under take-off distance constraints [1], increasing the maximum lift coefficient of the wing was considered more advantageous than increasing wing area, which would have introduced additional structural mass and cruise drag.

Several flap concepts were considered during the preliminary stage, namely a plain flap, a single-slotted flap, and a Fowler flap. This mechanism provides a stronger lift increase than simpler alternatives by combining an increase in effective camber with an increase in effective aerodynamic chord. This makes it particularly suitable for the present aircraft, where the objective was to improve take-off capability while preserving an efficient wing for the distance segment.

The final geometry was developed from the “Super” wing airfoil as a main-element–flap arrangement with a dedicated deployed position, shown in Figure 4. The adopted configuration uses a flap-to-chord ratio of $c_f/c_{root} = 0.32$, a take-off deflection of $\delta_f = 14°$, a nominal gap of $g/c_{root} = 0.03$, and a zero-overlap arrangement. In the present notation, both gap and overlap are defined with respect to the root chord. When deployed, the flap increases the effective local chord by approximately 12%.

From a spanwise point of view, the Fowler flap was applied only to the central wing panel. It is worth mentioning that extending the mechanism to the outer panels would have introduced substantially higher geometric, structural, and actuation complexity, especially near the elliptical wing-tip region. After considering both aerodynamic benefit and integration constraints, the central panel was identified as the most effective location, capturing the main take-off benefit while keeping the system mechanically manageable.

For cruise flight, the flap is set to $\delta_f = -2°$, which slightly reduces the effective camber and effective chord of the airfoil and was adopted to decrease the cruise drag coefficient once the additional lift is no longer required. For climb, an additional configuration was analysed at the representative climb condition, corresponding to $\alpha_{climb} = 3.5°$ and $V_{\text{climb}} = 18.5\,\text{m/s}$. Several guide positions were tested in order to evaluate the effect of the Fowler kinematics on the climb aerodynamic performance. The best compromise was obtained for a guide position of 72%, which was therefore retained for the final mechanism definition.

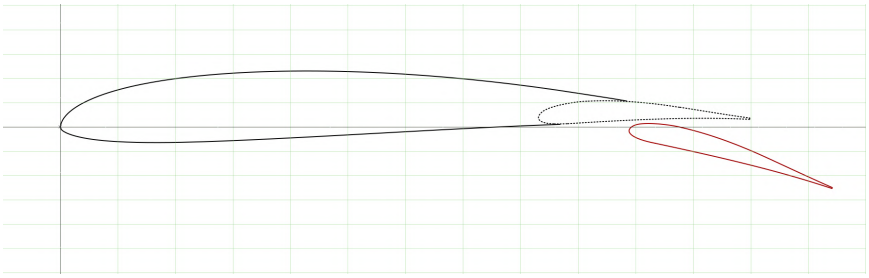


Figure 4: Take-off and cruise configuration of the adopted Fowler flap.

Table 6: Fowler flap parameters.

Parameter	Symbol	Value
Flap/chord ratio	c_f/c_{root}	32%
Take-off	δ_f	14°
Cruise	δ_f	$-2°$
Gap	g/c_{root}	3.0%
Overlap	o_l/c_{root}	0%
Chord increase	$\Delta c/c_{root}$	12%

The aerodynamic comparison between the baseline "Super" airfoil and the plain flap was obtained in *XFLR5* [5], while the Fowler flap was assessed through two-dimensional CFD analyses performed using *ANSYS Fluent* [6]. To ensure consistency between both methodologies, the plain flap was also analysed in CFD and compared with the corresponding *XFLR5* result. The obtained difference was approximately 1.7%, which was considered negligible for the present design stage.

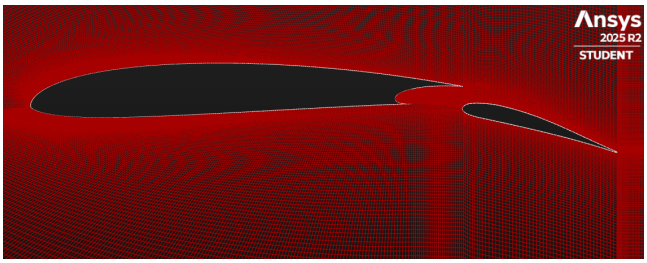


Figure 5: Computational mesh for flap analysis.

The CFD mesh used for the Fowler flap analysis is shown in Figure 5. Local refinement was concentrated around the airfoil, flap, and gap region, where the pressure gradients and slot-flow effects are more relevant, while the outer domain was kept coarser to reduce computational cost.

Results, shown in Figure 6, indicate that the Fowler flap provides the highest lift coefficient throughout the relevant take-off range, alongside a substantially higher peak value than both the baseline airfoil and the plain flap reference. In particular, the adopted configuration is expected to reach approximately $C_l \approx 2.34$ near the take-off angle of attack $\alpha_{T.O} = 9°$, which confirms the aerodynamic benefit of the concept.

The comparison between the three configurations is shown in Figure 6, indicating that the gain in lift obtained with the Fowler flap is sufficiently large to justify the additional mass and kinematic complexity of the system. In addition to the lift increase, the corresponding C_l/C_d trend was also considered as a complementary indicator of aerodynamic efficiency over the take-off range.

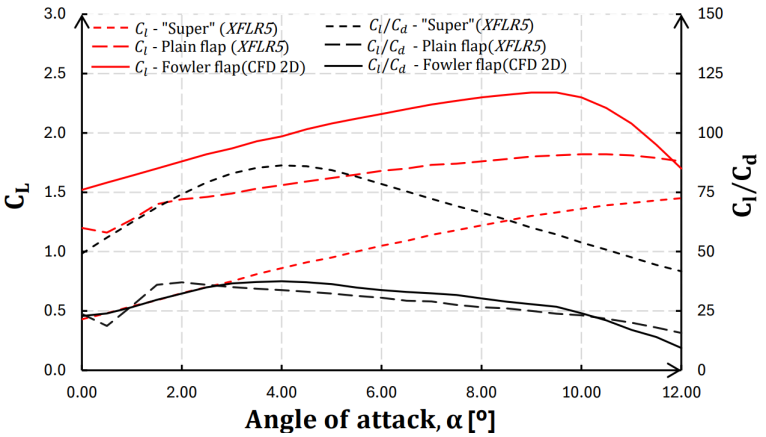


Figure 6: C_l–α and C_l/C_d comparison for the baseline "Super" airfoil, the plain flap and the Fowler flap configurations.

Although the Fowler configuration is not strongly penalized in terms of C_d in the present comparison, these drag-related results might appear optimistic due to being based on a two-dimensional CFD analysis. However, the lift advantage relative to both the baseline airfoil and the plain flap remains clear enough to support the selection of the Fowler concept. During cruise, the $-2°$ setting helps recover a lower-drag configuration, improving compatibility with the distance segment requirements.

2.4 Fuselage

2.4.1 Design Iterations

Several fuselage configurations were evaluated before converging on the final concept, with payload integration and aerodynamic efficiency as the main design drivers. To ensure a fair comparison between iterations, all configurations presented in this section were analyzed under identical conditions: reference wing area, flight speed and payload capacity. Therefore, CFD comparisons were performed for $S_{ref} = 0.794$ m^2, $V = 30$ m/s, and an 8-can payload configuration. This section focuses only on fuselage concept evolution; the influence of flight speed and number of cans on the final fuselage drag is addressed separately in Section 2.4.2.

The first iteration, shown in Figure 7, adopted vertically oriented cans distributed over two vertical levels. Each level contained a 2×2 arrangement, resulting in a stacked payload layout inside the fuselage. Although this solution allowed compact longitudinal packaging, it significantly increased fuselage height and frontal area, leading to a less favorable aerodynamic shape. Drag decomposition confirms this behavior: this iteration presented the highest pressure drag coefficient, $C_{Dp} = 4.50 \times 10^{-4}$, indicating stronger pressure losses associated with external geometry. Aft-body shape also presented a relatively abrupt reduction in cross-sectional area, promoting adverse pressure gradients and increasing the likelihood of flow separation [13]. In addition, this configuration presented a skin-friction drag coefficient of $C_{Df} = 1.37 \times 10^{-3}$, resulting in the highest total drag coefficient, $C_D = 1.82 \times 10^{-3}$.

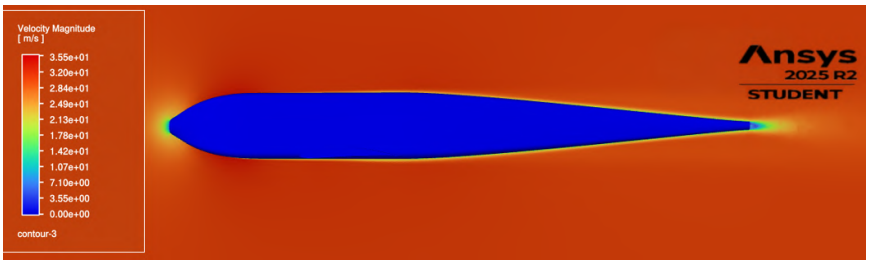


Figure 7: First fuselage iteration.

In the second iteration, presented in Figure 8, cans remained vertically oriented, but payload was rearranged into a single vertical level with a 2×4 layout. This modification reduced fuselage height and frontal area compared to the stacked configuration, improving overall aerodynamic shape. However, motor placement in the upper forward region introduced a local disturbance in the incoming flow and contributed to pressure drag near the nose region. Even with this limitation, improved packaging reduced pressure drag to $C_{Dp} = 3.96 \times 10^{-4}$, while skin-friction contribution also decreased to $C_{Df} = 1.30 \times 10^{-3}$. Total drag coefficient was consequently reduced to $C_D = 1.70 \times 10^{-3}$, confirming a clear aerodynamic improvement over the first iteration.

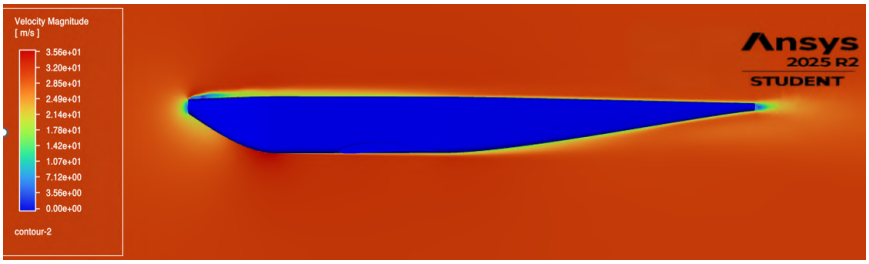


Figure 8: Second fuselage iteration.

The final 8-can concept, shown in Figure 9, maintained a single-level 2×4 payload layout, but cans were rotated into a horizontal, laid-down orientation. In addition, the motor was repositioned closer to the fuselage centerline, reducing the upper-nose flow disturbance observed in the second iteration and improving overall external integration. This change allowed a lower and more streamlined fuselage geometry,

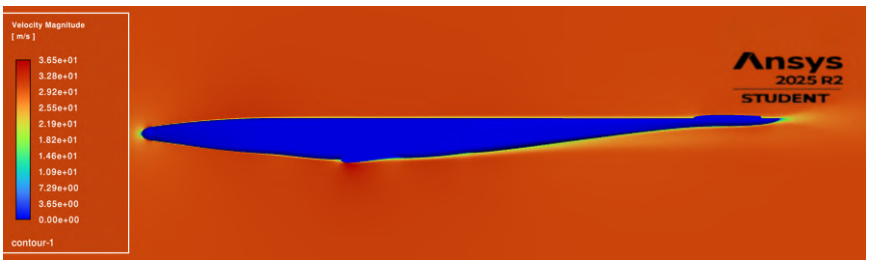


Figure 9: Final 8-can fuselage concept.

reducing frontal area without changing payload capacity. Improvement is particularly evident in pressure drag, which decreased to $C_{Dp} = 1.95 \times 10^{-4}$, less than half of the value obtained in the first iteration. Skin-friction drag also decreased to $C_{Df} = 1.18 \times 10^{-3}$, resulting in the lowest total drag coefficient among the three concepts, $C_D = 1.38 \times 10^{-3}$.

Overall, results show a progressive aerodynamic improvement across fuselage design iterations. Moving from a stacked vertical arrangement to a single-level configuration reduced frontal area, while rotating cans into a horizontal orientation and repositioning the motor closer to the fuselage centerline provided the most significant reduction in pressure drag. The final 8-can concept therefore represents the best aerodynamic baseline among the analyzed configurations and was selected as the basis for the subsequent payload-capacity study.

2.4.2 Drag Characterization

After selecting the final fuselage configuration, a set of aerodynamic analyses was conducted to quantify its drag contribution. The main objective was to determine the drag as a function of flight speed and number of cans, enabling its integration into the aircraft sizing process.

A study domain was first defined, covering the expected operational range of the aircraft in terms of velocity and payload configurations. This domain was selected to encompass the widest possible range of realistic operating conditions, ensuring that the resulting model would be applicable throughout the design space.

Within this domain, a series of discrete CFD simulations were performed at selected operating points. The study covered payload configurations ranging from 6 to 20 cans, with increments of two, and flight speeds ranging from 10 to 40 m/s, with increments of 5 m/s. These points were strategically chosen to capture the variation of drag across the domain while maintaining a manageable computational cost.

The results obtained from these simulations were then used to interpolate and extrapolate the drag behavior for intermediate and non-simulated conditions, allowing the construction of a continuous drag model over the entire design space. The resulting trends are illustrated in Figure 10, where the drag is plotted as a function of speed for different payload configurations. As expected, the drag increases with both flight speed and number of cans. The increase with velocity follows the expected non-linear behavior associated with aerodynamic drag. Regarding the payload variation, it is important to note that the frontal area remains essentially constant, since the cross-sectional arrangement of the cans does not change. Instead, the observed increase in drag with the number of cans is primarily due to the increase in wetted area, as the fuselage becomes longer to accommodate additional payload. This results in higher skin friction drag, indicating that viscous effects dominate the variation between configurations.

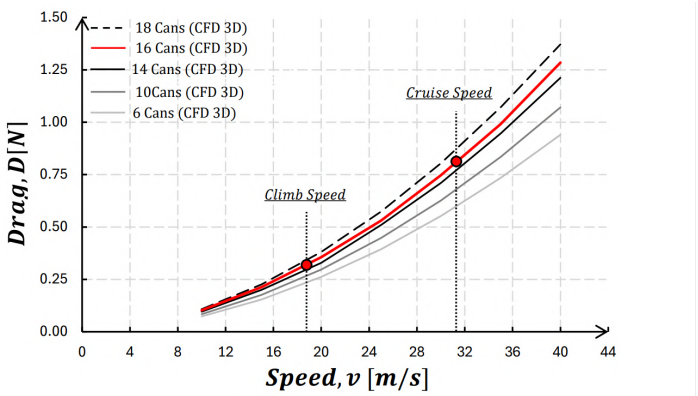


Figure 10: Fuselage drag as a function of flight speed for different payload configurations.

Finally, the processed data was implemented in the *Excel*-based sizing tool [4], allowing the fuselage drag contribution to be dynamically evaluated as a function of speed and payload during the aircraft design and optimization process.

2.5 Wing Selection

The wing selection was carried out through an *Excel*-based parametric sizing process [4], aimed at determining the span and reference chord that maximized the aircraft final score [1] while satisfying take-off, climb, cruise

and packaging constraints. Since a semi-elliptical wing had already been selected at the conceptual stage, this phase was mainly devoted to sizing the wing and comparing the corresponding aircraft configurations. The independent geometric variables were the wing span, b, and the reference chord, c. In parallel, the sizing loop also compared the optimal, three- and five-panel wings, plain and Fowler flaps, fixed and retractable landing gear, one- and two-motor arrangements, and different propeller selections. For each configuration, the wing area, aspect ratio, structural mass, and drag contributions were updated, using interpolated airfoil polars, span- and chord-dependent Oswald factors, and simplified weight models corrected with data from previous aircraft and from the first prototype.

Payload was treated as the main iterative variable. For each configuration, payload mass was increased until the take-off distance reached the chosen limit, using a semi-empirical take-off model corrected with prototype flight-test data. The distance segment was modelled as level flight in a circular path with constant bank angle. The results showed that using the full $60\,\mathrm{m}$ take-off distance [1] and carrying more payload was consistently more advantageous than targeting the short take-off bonus. The best-performing region of the design space was associated with a single-motor configuration, Fowler flaps and retractable landing gear. The final wing selected at this stage was later refined during the wing optimization phase.

2.6 Wing Optimization

For the final optimization phase, the wing planform was refined using *XFLR5* [5], ensuring that all config urations were evaluated under the same wing reference area defined during the sizing phase. Based on aerodynamic studies and design experience from previous ACC editions, the semi-elliptical configuration was selected as the most suitable compromise between aerodynamic performance and manufacturability. This configuration provides a lift distribution closer to the ideal elliptical behavior rather then a rectangular wing, leading to reduced induced drag and improved efficiency, while remaining simpler to manufacture than a fully elliptical planform.



Figure 11: Wing geometry.

As shown in Figure 11, the final geometry consists of a three-panel wing, composed of a rectangular central section and elliptical outer panels. This layout simplifies the structural integration at the wing root while improving the aerodynamic behavior along the outer span. An iterative geometric adjustment was performed to ensure chord continuity between sections while maintaining the total wing area constant.

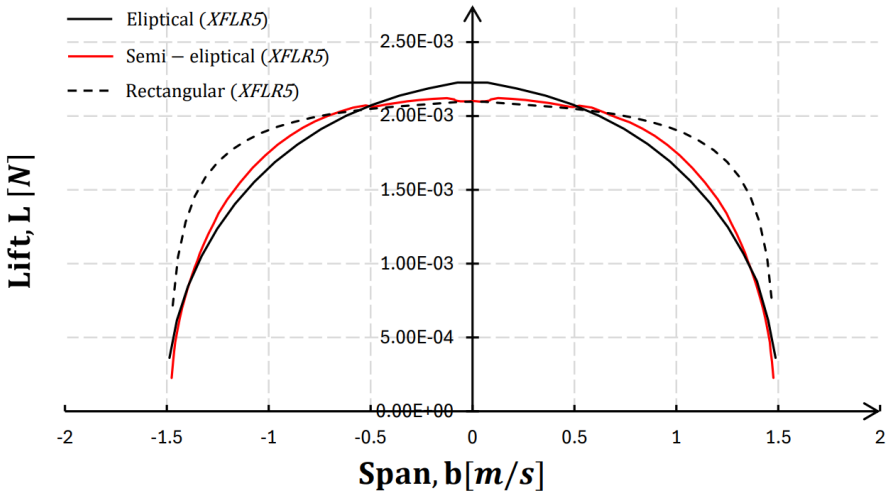


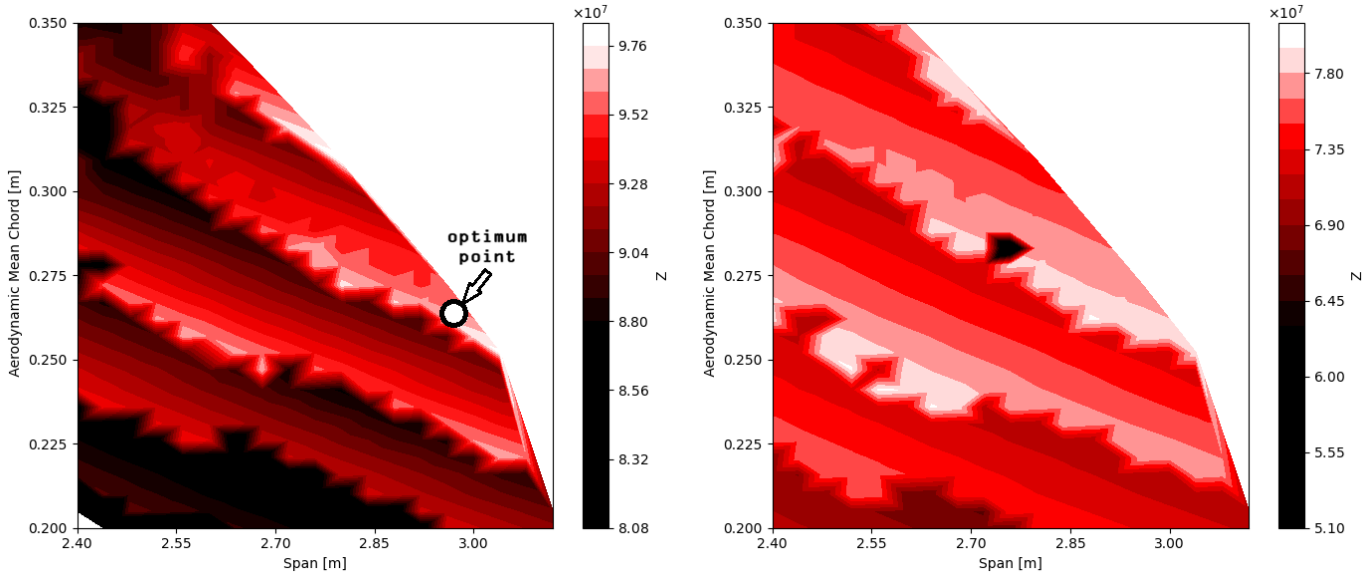
Figure 12: Semi-elliptical wing lift distribution.

The aerodynamic results confirm that the selected configuration produces a smoother spanwise lift distribution, as shown in Figure 12, particularly near the outer panels, reducing lift concentration at the tips and consequently lowering induced drag. Overall, the final wing geometry represents a well-balanced solution between aerodynamic efficiency, structural simplicity, and manufacturability.

2.7 Design Results and Payload

The final aircraft configuration resulted from the combined outcome of the previous aerodynamic analyses, namely the airfoil screening, the parametric wing-sizing loop, the semi-elliptical wing optimization, the flap assessment and the fuselage integration studies. The objective at this stage was to identify the wing size and number of cans, that maximized the expected ACC2026 score [1] while remaining sufficiently robust after the prototype corrections.

The main conclusions of the final sizing process are summarized in Figure 13, which compares the score maps obtained for the 60 and 40 m take-off cases as functions of wing span and mean aerodynamic chord.



(a) 60 m take-off case.

(b) 40 m take-off case.

Figure 13: Raw score distribution as a function of wing span and mean aerodynamic chord.

As shown in Figure 13, the 60 m take-off case reaches a higher maximum raw score than the 40 m case, mainly because it allows larger payload values. However, the 40 m case presents broader regions of comparatively good performance, although with a lower absolute score ceiling. Figure 13 also shows that the selected geometry is located inside a competitive region of the 60 m design space rather than at an isolated singular optimum, which was considered advantageous from the point of view of robustness against modelling uncertainty and mass deviations.

Table 7: Final aircraft configuration and main performance results.

Wing		Config.		Payload		Perf.	
Airfoil	"Super"	Layout	Low-wing	Theoretical	16 cans	Take-off dist.	55 m
Span	2.92 m	Flap	Fowler	Real	14 cans	Stall speed	9.27 m/s
Chord	0.272 m	Gear	Retractable	Announced	12 cans	Cruise speed	34.0 m/s
Area	0.794 m^2	Prop.	13×9	Empty est.	3.722 kg	Climb speed	18.5 m/s
Aspect Ratio	10.74	Motor	1	Empty real	3.366 kg	Climb rate	0.98 m/s
Panels	3			Max take-off	8.908 kg		

The values reported in Table 7 should be interpreted as follows. The selected Fowler flap corresponds to the high-lift solution retained after the comparative aerodynamic assessment, since it provided the largest take-off benefit and was therefore adopted in the final configuration.

The value $S_{TO} = 55$ m refers to the predicted take-off distance of the theoretical 16-can configuration obtained from the final sizing model. In the payload column, "Theoretical" denotes the maximum payload geometrically compatible with the aircraft and associated with the mathematically best design point, "Real" denotes the maximum payload safely demonstrated in representative prototype flight tests, and "Announced" denotes the payload declared by the team for the competition.

In the present case, the theoretical payload remained 16 cans, while prototype testing showed that 14 cans was the maximum payload that could be operated safely within the intended take-off margin. Thus, the announced payload was fixed at 12 cans.

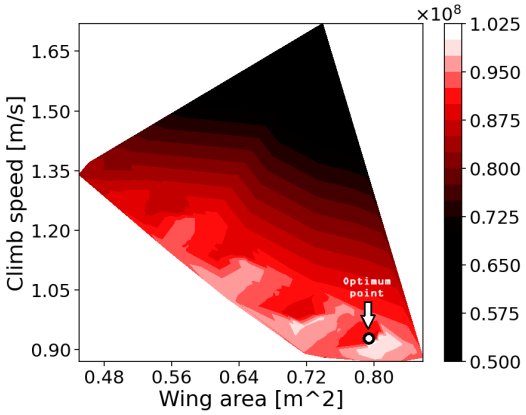


Figure 14: Raw score, climb rate versus wing area.

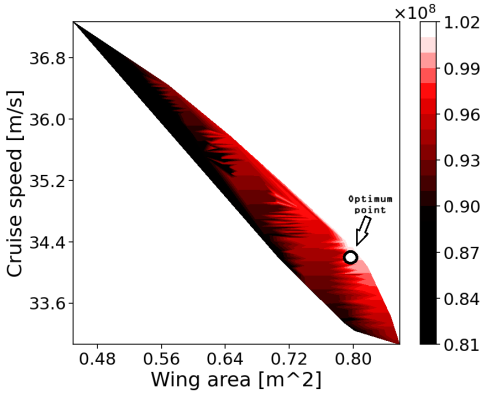


Figure 15: Raw score, cruise speed versus wing area.

The influence of the main mission-performance variables on the final score is further illustrated in Figures 14 and 15, which shows the score maps for climb rate and cruise speed. As shown in Figure 15, the final aircraft was not selected by maximizing a single metric in isolation. In both maps, the highest-scoring region is associated with a balanced compromise between performance variables rather than with the absolute maximum of cruise speed or climb rate alone. This behavior is fully consistent with the final design choice, which prevails a competitive and experimentally supported configuration over a narrower optimum more sensitive to modelling or manufacturing deviations. In summary, the aerodynamic analyses consistently converged to a low-wing, semi-elliptical aircraft equipped with a Fowler flap and retractable landing gear. Optimized for the 60 m take-off case and subsequently corrected through prototype testing, the final aircraft was selected as the most competitive and experimentally supported configuration obtained from the complete design process.

2.8 Stability and Control

The empennage configuration was defined to maximize aerodynamic efficiency while ensuring adequate static and dynamic stability throughout the full loading envelope. Following the experience from previous ACC editions, the V-tail configuration, including the use of an elliptical planform, did not introduce significant manufacturing difficulties. Therefore, an elliptical V-tail was adopted to take advantage of its improved lift distribution and reduced induced drag. Additionally, due to the use of an all-moving tail, the selected airfoil had to accommodate the internal rotation mechanism while maintaining good structural integrity and low aerodynamic drag. For this reason, the NACA 0008 airfoil was selected, providing sufficient internal thickness for the pivot system without significantly penalizing aerodynamic performance. The resulting V-tail configuration is shown in Figure 16, while its main geometrical parameters are presented in Table 8.

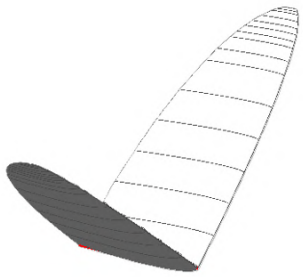


Figure 16: V-tail geometry.

Table 8: Geometrical parameters of the V-tail.

Parameter	Value
Configuration	All-moving elliptical V-tail
Airfoil	NACA 0008
Span (one surface)	0.395 m
Mean aerodynamic chord	0.132 m
Aspect ratio (one surface)	3.0
Dihedral angle	35.2°
Setting angle	-1.15°
Tail arm	1.194 m

2.8.1 Static Stability

The static stability analysis was carried out in *XFLR5* [5], considering the most critical center of gravity positions resulting from the internal arrangement of the payload cans and onboard components. The aircraft was intentionally designed so that the payload is positioned as close as possible to the main wing spar region, minimizing the center of gravity variation between different loading configurations.

As summarized in Table 9, the center of gravity varies only between 0.121 m and 0.123 m, while the neutral point remains approximately constant at 0.158 m. This leads to a static margin ranging between 12.9% and 13.9%, showing only a limited variation as the number of cans changes. This confirms that the aircraft preserves consistent longitudinal handling qualities across the full loading envelope.

Regarding lateral-directional stability, a 4° dihedral angle was intentionally introduced in the tip wing panels to improve the restoring rolling moment under sideslip conditions. This directly contributes to a more negative C_{l_β}, increasing lateral stability. In parallel, the V-tail geometry provides positive directional stability, reflected in the positive values of C_{n_β}, as also presented in Table 9. These results confirm that the aircraft is statically stable in both longitudinal and lateral-directional axes for all loading conditions.

Table 9: Static stability analysis.

Parameter	Aft CG	Forward CG	Requirement	Interpretation
X_{CG} [m]	0.123	0.121	$X_{CG} < X_{NP}$	Stable
X_{NP} [m]	0.158	0.159	Reference	Neutral point
Static Margin [%]	12.9 (12 cans)	13.9 (6 cans)	Positive	Stable
C_{l_β}	-0.001	-0.0011	Negative	Laterally stable
C_{n_β}	0.0007	0.0008	Positive	Directionally stable

2.8.2 Dynamic Stability

Dynamic stability analyses were carried out in *XFLR5* [5] for the most critical loading condition and confirms adequate aircraft response in all principal flight modes. As summarized in Table 10, the longitudinal response shows that the short-period mode presents a damping coefficient of 0.741, indicating a strongly damped pitch response and rapid recovery after disturbances. The phugoid mode presents a damping coefficient of 0.0497, which is expected for a low-frequency energy exchange mode and remains dynamically stable.
For the lateral-directional response, the rolling mode presents a very fast characteristic response time of 0.0161 s, confirming strong roll damping. The Dutch roll mode presents stable oscillatory behavior with a damping coefficient of 0.135 and a natural frequency of 1.227 Hz.
The spiral mode presents a time to double amplitude of 284 s, indicating an extremely slow divergence. Although formally slightly unstable, this value demonstrates that the aircraft remains practically stable over the mission flight duration and can be easily corrected by minor pilot input, as reflected in Table 10.

Table 10: Dynamic stability analysis.

Stability	Type	Parameter	Value	Interpretation
Longitudinal	Phugoid	Damping Coefficient	0.0497	Stable, lightly damped
	Short Period	Damping Coefficient	0.741	Fast pitch recovery
Lateral	Spiral	T_2 [s]	284	Very slow divergence
	Rolling	T [s]	0.0161	Very fast damping
	Dutch Roll	Damping Coefficient	0.135	Stable oscillatory mode
		Natural Frequency [Hz]	1.227	Acceptable lateral response

Overall, the aircraft demonstrates adequate dynamic stability characteristics, ensuring predictable handling and robust behavior throughout the full mission envelope.

3 Payload Prediction

The payload prediction was based on the maximum payload mass of the aircraft under expected atmospheric conditions during the competition. Since the most limiting flight phase was identified as take-off, the prediction was obtained by estimating the payload that still allows a safe take-off.
The prediction combined propulsion data from wind tunnel tests of the motor/propeller system with the aerodynamic model used for aircraft sizing. Lift and drag polars obtained from ANSYS® and *XFLR5* were used together with the sizing spreadsheet to determine the payload mass. In the analyzed range, the obtained relation was approximately linear and can be expressed as:

$$Payload = 2.905\,\rho + 2.1987\ [\text{kg}] \qquad (2)$$

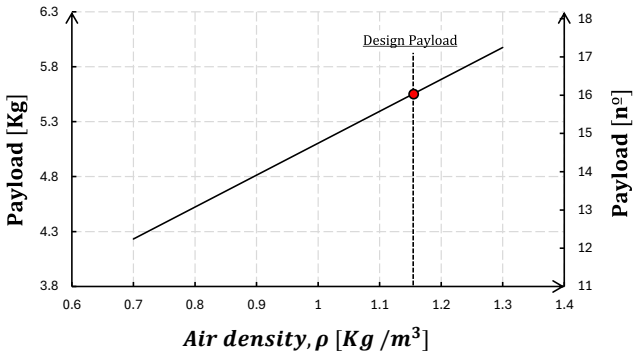


Figure 17: Payload as a function of air density.

where payload is the maximum take-off mass in kg and ρ is the air density in kg/m^3, as shown in Figure 17. After subtracting the estimated empty mass of the aircraft, equal to 3.4 kg, the corresponding payload was determined for representative density values.

4 Structural Design

The structural design of the aircraft relies predominantly on carbon fiber reinforced laminates for all primary load-bearing components, selected over glass fiber due to its lower density and superior stiffness and strength-to-weight ratio, despite its higher cost. Glass fiber was used in a small number of specific cases with the intent

to improve the surface finish of the outer skin, with any structural contribution being a secondary benefit rather than the main design driver. Core materials were chosen on a case-by-case basis, according to the specific requirements of each component. To ensure the fidelity of the ANSYS® [6] numerical models, representative material properties were obtained experimentally by testing carbon fiber reinforced specimens in a universal testing machine, determining key properties such as tensile strength (σ_u) and Young's modulus (E), following ASTM D3039/D3039M [15], and shear modulus (G), maximum shear stress, and shear strain (τ_{max} and γ_{max}), following ASTM D3518/D3518M [16]. All composite structural analyses presented in this chapter were performed using the ANSYS® [6] Composite PrepPost (ACP) module to define the laminate lay-up and fibre orientations.

A load factor of $n = 3$ was applied to all flight load cases, combined with a structural safety factor of 1.5 and a manufacturing factor of 1.25, accounting for the inherent variability in wet layup composite manufacturing processes. For the asymmetric landing case, and for the landing gear structural sizing as a whole, a dedicated ground load factor of $n_g = 4$ was adopted, due to the fact that it is more difficult to predict the landing loads through analytical methods than quasi-static aerodynamic loads.

4.1 Wing Structure

The wing structure follows a conventional layout consisting of a single main spar, a sandwich skin, and internal structure, as illustrated in Figure 18. This configuration was selected based on experience from previous editions and was optimized to achieve the best possible stiffness-to-weight ratio. The spar web, spar caps, and skin were sized through an iterative calculation process implemented using an *Excel* [4] spreadsheet, in which the structure was idealized according to the following load-carrying assumptions: the spar web resists all shear forces under the most critical flight conditions; the spar caps carry the bending moments; and the sandwich skin resists the torsional moment induced by the aerodynamic surfaces.



Figure 18: Wing structural layout.

Three critical flight load cases were considered in the structural sizing, as shown in Figure 19: the cruise flight condition, corresponding to the design cruise speed with maximum payload and representing the primary aerodynamic load case; the wing-tip static load test, in which a concentrated load is applied at the wing-tip, replicating the mandatory static structural test required by the competition regulations [1]; and the asymmetric landing, in which the aircraft touches down on a single landing gear leg, transferring the full structural loads into the main spar and representing the most demanding load case for the inboard spar region.

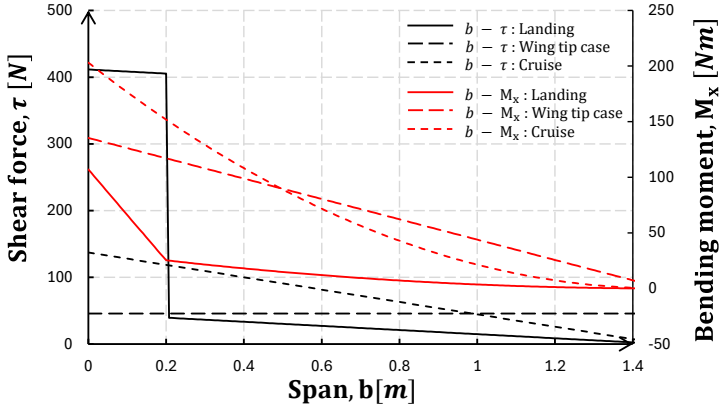


Figure 19: Shear force and bending moment distributions along the half-span.

To determine the number of wing and fuselage sections required, as well as the stowage arrangement, the available volume within the transport box was taken into account. A packing routine was integrated directly into the sizing spreadsheet, enabling automatic and iterative evaluation of different stowage configurations for both the fuselage and the wing. The routine always prioritized the minimum number of component parts compatible with the box envelope. As a result, a three-section wing and a three-section fuselage was adopted, as shown in Figure 20, yielding a final transport box of $987 \times 318 \times 194$ mm (length $\times$ height $\times$ width).



Figure 20: Transport box stowage arrangement.

The iterative sizing procedure was applied independently to each panel, allowing for a lighter structure in the wing-tips, where the applied loads are significantly lower, without compromising structural performance in the higher-loaded inboard region. The final laminate layup for each wing panel is summarized in Table 11.

Table 11: Wing laminate layup for central and tip panels.

Panel	Component	Core Material	Composite Skin
Tip panels	Spar	Rohacell® (10 mm)	Carbon fiber 90 g/m^2 ($\pm 45°$)
Tip panels	Skin	Balsa wood (1 mm)	Carbon fiber 11 g/m^2 ($\pm 45°$)
Central panel	Spar	Rohacell® (10 mm)	Carbon fiber 2 × 200 g/m^2 ($\pm 45°$)
Central panel	Skin	Balsa wood (1 mm)	Carbon fiber 20 g/m^2 ($\pm 45°$)

From the laminate thicknesses and material densities obtained above, the theoretical wing mass per unit span was calculated analytically. To improve the reliability of this estimate, the wings manufactured in previous competitions that were sized using a comparable methodology, were weighed and the measured masses were compared against the corresponding theoretical predictions. This calibration exercise yielded a correction factor of $k_w = 1.244$, which was applied to the current theoretical weight to obtain the final wing mass estimate.
A circular configuration was selected for the wing panel connections instead of a quadrangular one, as it promotes a more uniform stress distribution and reduces stress concentrations, resulting in a more structurally efficient joint. In addition, this geometry allows a more consistent fit between mating parts with reduced play, whereas quadrangular sections are more difficult to manufacture to tight tolerances, leading to larger gaps at the interface and consequently less precise assembly.
The connection length was set to 80 mm for each panel, rather than 40 mm, after preliminary tests showed that the shorter alternative was more susceptible to small geometric imperfections, leading to slight clearance between the male and female components. Increasing the overlap length reduced these gaps and improved the overall stability and fit of the joint. The female connector was thus analyzed and defined with seven layers of 318 g/m^2 carbon fibre sleeve, selected as it represents the closest commercially available areal weight, and a total length of 80 mm.

4.2 Nose, Central Fuselage and Payload

4.2.1 Nose Module

The nose module houses the propulsion and avionics systems, utilizing a skin made of glass fiber and carbon fiber. The internal support consists of a Rohacell® tray with one layer of carbon fiber on each face, optimized

with cutouts to reduce weight and secure the electronics.
The structure includes two frames: one made of plywood to withstand motor loads and a rear one made of Airex® (with a layer of carbon fiber on each side), designed to transfer the motor loads and electronics weight to the central fuselage. To ensure signal integrity and compliance with regulations [1], the measuring box is elevated with side supports, preventing blockage from the upper carbon fiber layers. This integration eliminates the need for a removable hatch, ensuring weight savings and a smooth aerodynamic transition. The final layup for the nose module is listed in Table 12.

Table 12: Material composition of the nose module.

Component	Core Material	Composite Skin
Nose Skin	-	Glass fiber 48 g/m^2 (0/90°) + Carbon fiber 200 g/m^2 (0/90°)
Avionics Tray	Rohacell®	Carbon fiber 90 g/m^2 (0/90°)
Front Frame	Plywood	-
Rear Nose Frame	Airex®	Carbon fiber 90 g/m^2 ($\pm$45°)

4.2.2 Central Fuselage and Payload



Figure 21: Payload tray integration.

The central fuselage geometry was designed to satisfy the requirements described in Section 2.1, serving as the primary load-bearing spine of the aircraft, while the top access hatch was designed to maximize the effective carbon fiber area available to resist structural loads without compromising loading efficiency. The baseline fuselage skin layup consists of an outer 48 g/m^2 glass fiber layer ($0/90°$), followed by a 90 g/m^2 carbon fiber layer ($\pm 45°$), then a 90 g/m^2 carbon fiber layer ($0/90°$) and finally a 200 g/m^2 carbon fiber layer ($0/90°$). This layup configuration was adopted to achieve the required torsional resistance while maintaining adequate impact durability and bending stiffness. During flight, the payload must remain absolutely static to prevent center of gravity shifts during critical flight phases, so a dedicated structural tray was designed to support the cans while also ensuring they do not contact each other, as required by the competition regulations [1], as seen in Figure 21. Following an iterative process, the tray layup was established as a sandwich with 200 g/m^2 carbon fiber layer on each side and an 18 mm-wide longitudinal unidirectional carbon fiber strip running between the cans for additional bending stiffness. As the tray still exhibited considerable deformation, three transverse frames were added, reducing it to acceptable levels. Foam inserts integrated into the top hatch apply a compressive reload to the payload when closed, preventing vertical movement. The central section also provides the structural interface for the low-wing configuration, directly transferring spar loads into the reinforced internal frames. The nose and aft fuselage connection with the central fuselage, were carefully analyzed to ensure alignment, where three M3 bolts are used to fasten fuselage sections. The nose frame, which uses an Airex® foam core, required plywood inserts around the bolt holes to prevent core crushing under bearing and fastening loads, a reinforcement not needed at the aft fuselage connection where a full plywood core already provides sufficient compressive strength.

4.2.3 Fuselage FEA Validation

To validate and optimize the structural layups of the nose module and central fuselage, Finite Element Analyses (FEA) were carried out using the Static Structural module of ANSYS® [6]. For the nose module, the applied loads comprised a tensile force of 21.75 N, a component weight of 41.75 N, and a moment of 535.5 N·m representing the motor torque, with a fixed support condition imposed at the connection to the central fuselage section.

The central fuselage simulation considered the payload weight under the corresponding load factor, resulting in an applied load of 247.13 N, together with structural transfer loads, including the bearing and axial loads transmitted from the nose and aft fuselage, with a fixed support condition imposed at the connection between the central fuselage and the wing. In both cases, the Tsai-Wu [8] and Tsai-Hill [9] failure criteria were evaluated across all plies. Neither component exhibited failure, confirming the adequacy of the selected layups. The governing design criterion therefore became total deformation.

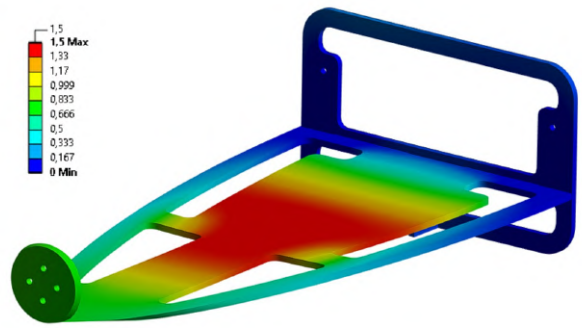


Figure 22: Nose Module deformation analysis (mm).

The nose module did not show significant deformation under the applied loads, with a maximum displacement of 1.50 mm, as seen in Figure 22, remaining below the limit 3 mm defined during the initial design phase to ensure that the measurement box and electronic components remain sufficiently constrained. For the central fuselage, the introduction of three transverse frames beneath the payload tray drastically reduced the peak deformation to 3.24 mm, as seen in Figure 23. The value is acceptable since the minimum clearance between the cans and the fuselage skin is 5 mm, confirming that the payload never contacts the structural skin under load, thus avoiding any risk of damage to the cans or the fuselage.

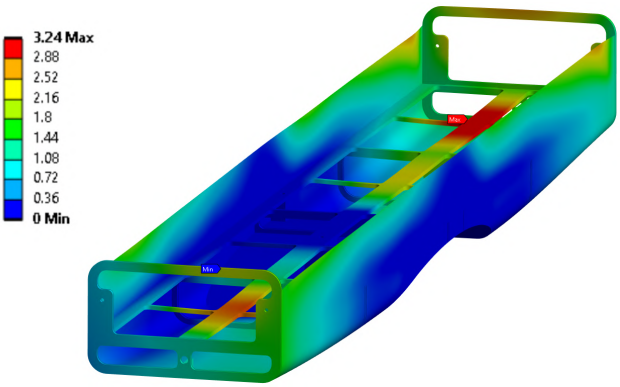


Figure 23: Central fuselage deformation analysis (mm).

4.3 Aft Fuselage and Empennage

4.3.1 Design and Materials

The aft fuselage was designed to minimize the number of parts while maximizing ease of assembly for both the empennage and the connection to the central fuselage section, the latter being made as described in Section 4.2.2. The connection between the V-tail and the aft fuselage was established through a concentric carbon fiber tube interface designed to provide both the rotation axis and structural load-transfer. In this configuration, represented in Figure 24, an 8 mm diameter tube integrated into the aft fuselage receives a 6 mm diameter tube integrated into the empennage, thereby forming the pivoting joint. Although this approach adds manufacturing complexity, it was the simplest way to ensure the empennage seated into the aft fuselage with minimal play. Since no internal frames or additional tubes are placed along the aft fuselage length, and

the skin consists solely of one carbon fiber and one glass fiber ply, buckling became a concern. To address this without requiring additional frames, an omega-shaped stiffener made of one layer of 200 g/m^2 carbon fiber was bonded along the lower full length of the aft fuselage, together with unidirectional carbon fiber strips at $+45°$, $-45°$ and $0°$, providing the necessary resistance to buckling with minimal weight penalty. The empennage was sized using the same iterative spreadsheet methodology described in Section 4.1, adapted for the load cases applicable to the tail surfaces, resulting in an extremely light yet robust structure. To size the all-moving V-tail mechanism, a dedicated worksheet was integrated into the same spreadsheet, working in parallel with the aerodynamic calculations to ensure that the selected airfoil section provided sufficient internal space for the actuation mechanism, and to determine the optimal servo position and moment arm relative to the aerodynamic center, minimizing the hinge moment and therefore the servo force required.

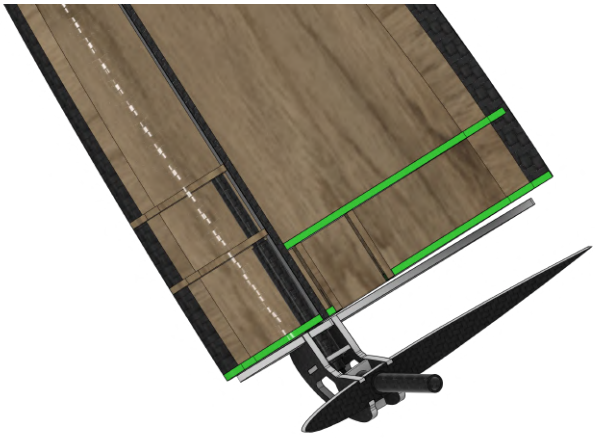


Figure 24: Empennage - aft fuselage connection.

Table 13: Material composition of the aft fuselage and empennage components.

Component	Core Material	Composite Skin
V-Tail Skin	Balsa	Carbon fiber 11 g/m^2 ($\pm 45°$)
V-Tail Spar	Rohacell®	Carbon fiber 20 g/m^2 ($\pm 45°$)
V-Tail Ribs	Rohacell®	Carbon fiber 90 g/m^2 ($\pm 45°$)
Aft fuselage Skin	—	Glass fiber 48 g/m^2 (0/90°) + Carbon fiber 200 g/m^2 (0/90°)
Front/Rear Frames	Rohacell® (3 mm)	Carbon fiber 90 g/m^2 ($\pm 45°$)

4.3.2 Aft Fuselage FEA Validation

To validate the aft fuselage structure, a Static Structural and Eigenvalue Buckling analysis was carried out in ANSYS® [6] under the critical load case, comprising a vertical force of 27.56 N, a lateral force of 20.23 N, and a torsional moment of 4.05 N·m, all applied at the empennage connection to the aft fuselage, with a fixed support condition imposed at the interface between the aft fuselage and the central section. The Tsai-Wu [8] and Tsai-Hill [9] failure criteria confirmed that the selected layup would not fail under the applied loads. Regarding deformation, while total deflection reached a maximum of 5.35 mm, as seen in Figure 25, well within the accepted limit of 10 mm, the most critical criterion is not deformation but rather the rigid body rotation of the tail surfaces, since any angular deviation directly affects the trim of the aircraft. The maximum rotation of the aft fuselage under the applied loads was found to be $1.85°$, a value the team considered acceptable as it is sufficiently small to produce no significant impact on the trim of the aircraft.

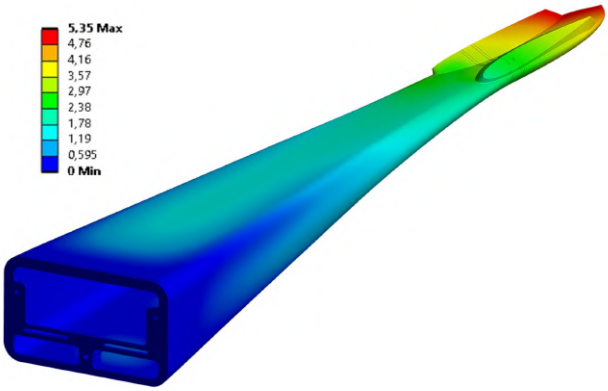


Figure 25: Aft fuselage deformation analysis (mm).

Given the absence of internal frames along the aft fuselage length, buckling was a structural concern, as discussed in Section 4.3.1. The Eigenvalue buckling analysis returned a first buckling load multiplier of 2.16, meaning the structure would buckle at 2.16 times the applied design load. This value is considered acceptable since, at that load level, the laminate would already have failed according to the Tsai-Wu [8] and Tsai-Hill [9]

strength criteria, meaning material strength is the active failure mode rather than structural instability. This confirms that buckling is not the critical failure mode and validates the effectiveness of the omega-shaped stiffener combined with the unidirectional carbon fiber strips, which together provided sufficient buckling resistance without the need for additional internal frames, as shown in Figure 26.

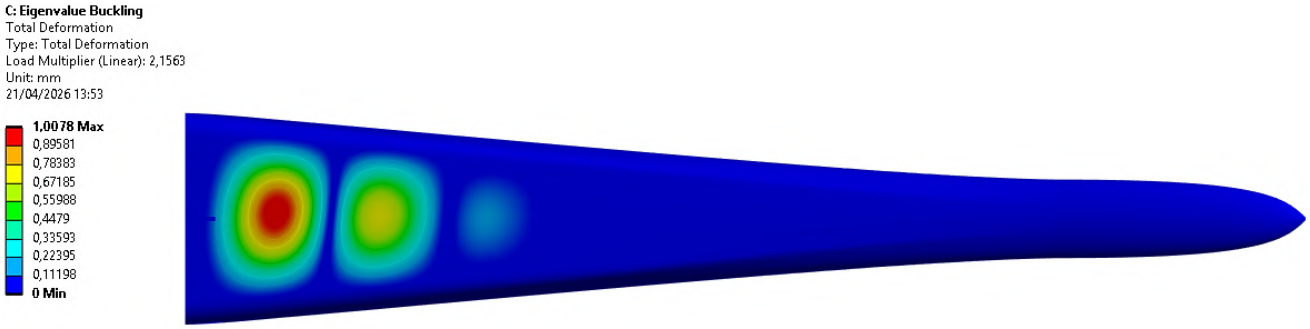


Figure 26: Eigenvalue Buckling Analysis (deformation in mm).

4.4 Landing Gear

The landing gear system was developed as a fully integrated structural and mechanical subsystem, designed to ensure reliable deployment, efficient retraction, and structural integrity under all expected operational loads. The present system relies on a compact rotational retraction mechanism driven by a linear actuator and a multi-link transmission system.

The design methodology combined iterative numerical simulations using ANSYS® [6], geometric optimization and experimental validation through real flight testing, ensuring both structural reliability and functional performance.

4.4.1 Main Strut and Linkage Mechanism

As a primary load-bearing element, the main strut is designed to withstand demanding conditions. An upper curvature was introduced to ensure proper kinematic alignment, promote smoother load transitions and reduce stress concentrations at the attachment region. Manufactured from composite materials and optimized through iterative ANSYS® [6] simulations, the structure is designed to resist the dominant longitudinal compression of landing and the secondary bending induced by the wheel offset, while localized stress concentrations arise at the pivot and axle connections. The retraction relies on a compact multi-link mechanism that converts the actuator's linear motion into the strut rotation, as shown in Figure 27. The linear actuator drives the first link, transmitting motion to an intermediate link rotating on a fixed pivot which, in turn, applies force to the final link to rotate the main strut.



Figure 27: Linkage mechanism.

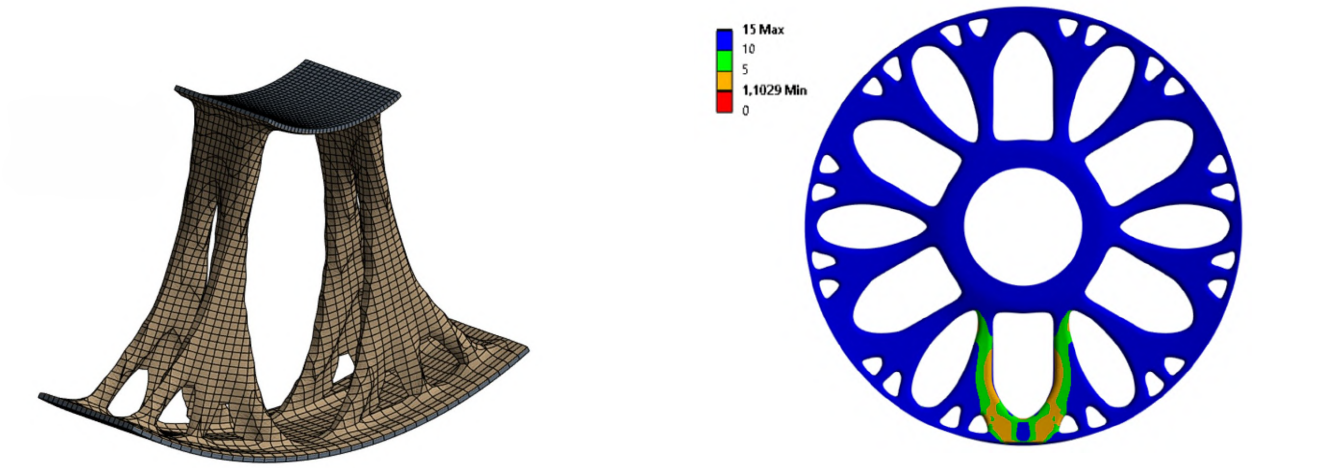
Structurally, the links primarily withstand longitudinal loads (tension, compression and bearing), while the pins withstand shear and bending stress. For added safety, the final link incorporates a mechanical stop to lock the system once deployed, effectively preventing unintended retraction under landing loads and ensuring that the actuator is not subjected to impact forces, which are instead transferred directly through the locked mechanical structure.

4.4.2 Wheel Design and Structural Validation

The wheel was developed as a structurally optimized and energy-absorbing component, combining topology-driven geometry with experimentally validated damping performance. The rim geometry was obtained through topology optimization under representative ground contact loads, starting from a 60° sector and replicated radially, as shown in Figure 28a. This resulted in a mass reduction of approximately 46% while preserving load paths and stiffness continuity.

Structural validation of the rim was performed through FEA, considering representative landing scenarios with a load factor and an embedded safety factor applied directly to the load cases. Multiple critical loading configurations were analyzed to capture the most demanding operational conditions.

Initially, an asymmetric load case was considered, consisting of a fully vertical force applied on a single wheel, representing a worst-case landing scenario. Subsequently, a more representative off-axis condition was introduced, corresponding to a 6.62° wing-tip contact angle. In this configuration, the resultant force was decomposed into two components: a vertical component associated with ground impact and a horizontal component. This multi-axial loading condition was found to be more critical, as it generates a combined stress state within the rim, significantly increasing local stress concentrations. The analysis enabled identification of critical regions, primarily at the connection between the wheel center and the structural arms connecting it to the rim, where load transfer is most severe, as illustrated by the topology-optimized geometry in Figure 28a. Results confirmed that stresses remain within admissible limits for Polyamide 6 (Nylon 6) reinforced with carbon fiber (PA6-CF), as shown in Figure 28b.



(a) Topology-optimized rim geometry.

(b) Static Structural analysis of the rim (Max equivalent stress safety factor).

Figure 28: Rim Analysis.

The tire design was driven by energy absorption requirements. Multiple internal architectures, as shown in Figure 29, were experimentally tested using a universal testing machine, with force–deformation curves used to quantify structural response, whose behavior is reflected in the comparative results presented in Figure 30. A normalized multi-criteria evaluation (mass, force at $\delta = 3$ mm, and resilience defined as the absorbed elastic energy) was applied to rank configurations. The honeycomb-based Thermoplastic Polyurethane (TPU) structure with 20% infill demonstrated the best overall trade-off, providing a balanced combination of strength, energy absorption, and damping capability, which improves impact mitigation and load distribution during landing.



(a) Honeycomb - 20% infill. (b) Honeycomb - 40% infill. (c) S - geometry. (d) L - geometry.

Figure 29: Infill geometries.

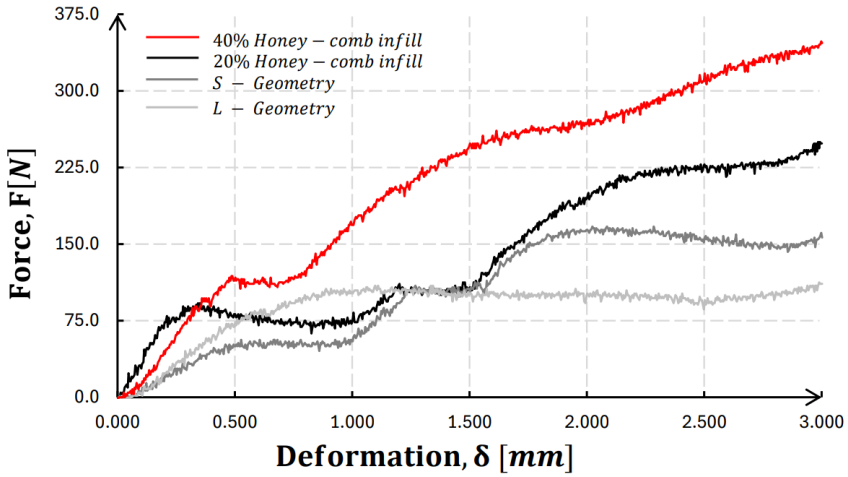


Figure 30: Force–Deformation response of tested tire architectures.

5 Propulsion System

As per the ACC2026 regulations [1], the aircraft must use a T-MOTOR 2814KV900 brushless motor with a current limit of 30 A. To determine the best propulsive configuration while strictly reducing potential point deductions, tests were conducted on a selection of propellers and LiPo batteries.

5.1 ESC Selection

The ACC2026 regulations impose a score penalty equation associated with exceeding the current limit [1]. To comply with this limitation, options to implement a current limiter were investigated. The evaluated solutions included an open-source Vedder Electronic Speed Controller (VESC) architecture and a Commercial Off-The-Shelf (COTS) electronic speed controller with programmable parameters.

After careful consideration, the team selected a Jeti® Model Mezon Evo ESC, which offered the possibility of tuning a wide range of complimentary motor parameters, such as the current limiter and timing, ensuring optimal system performance while remaining fully compliant with the competition regulations.

5.2 Propeller Selection

Initial theoretical evaluations were performed using the *AeroDesign Propeller Selector* [10] software. This preliminary analysis indicated that a two-bladed propeller with a pitch ranging between 10 and 13 in. would yield optimal performance.

To validate these results, experimental tests were conducted on the selected *Aeronaut* propellers using the university's wind tunnel. The analyses used a common 3S battery and the motor was capped at a maximum current of 30 A, aligning with the competition's 30 A current limit [1]. Testing was carried out across a range of freestream velocities up to 33 m/s. Data were recorded at velocity increments of 2.5 m/s, and at each target velocity, the motor was operated at full throttle to capture the corresponding performance metrics. The results are shown in Figure 31.

Using the findings obtained and the respective score given by the aircraft general performance spreadsheet, the selected propeller was an *Aeronaut* 13x9. Though the static thrust was lower than other options considered (14.1 N), the overall performance of this propeller was observed to be better over a greater speed range. At the maximum wind velocity analyzed, the motor produced 4.2 N, the second best performance at this velocity.

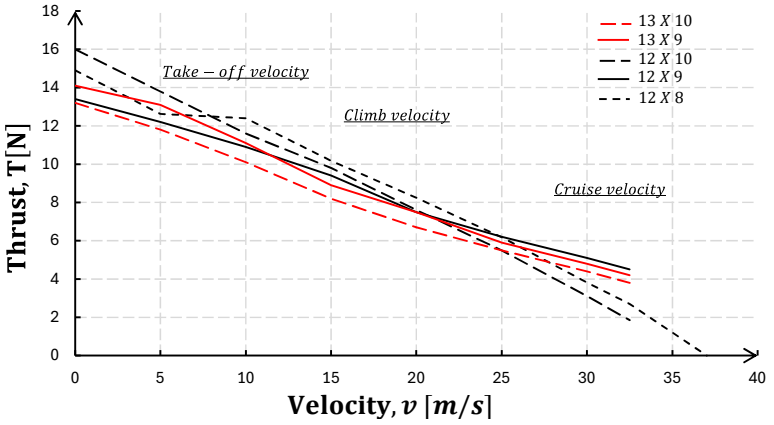


Figure 31: Thrust–Wind velocity analysis.

5.3 Main Battery Selection

To optimize the powertrain, wind tunnel tests were executed using the designated propeller and ESC to evaluate the performance and endurance of various candidate batteries. The endurance results are detailed in Figure 32.

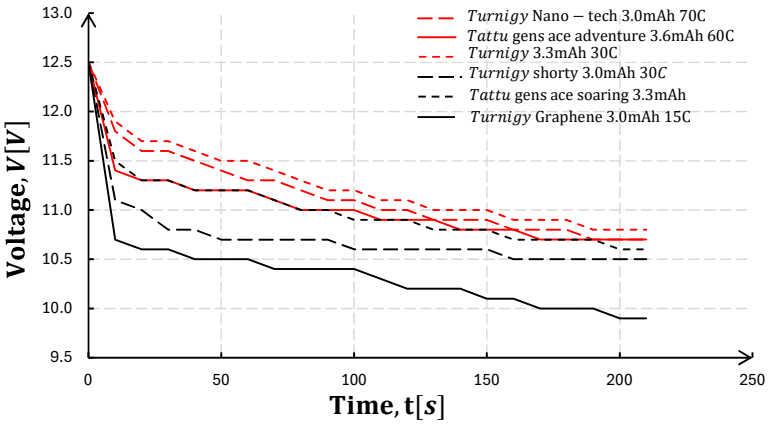


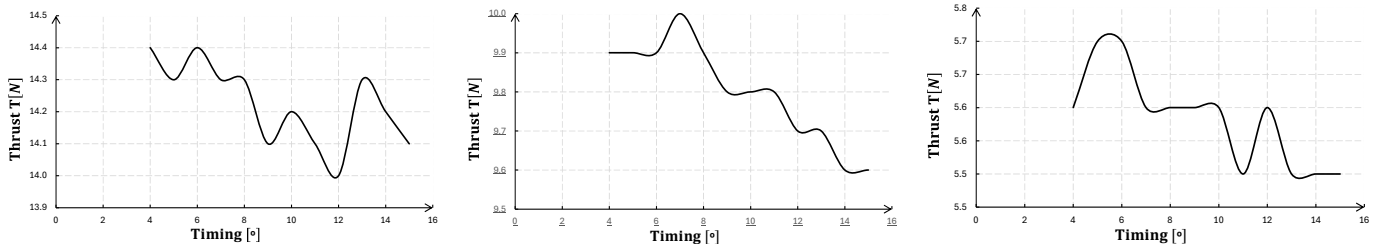
Figure 32: Battery endurance analysis.

Initially, a Turnigy® 3S 70C 3000 mAh LiPo battery was selected. This assumption relied on a safety factor of 1.23, which was calculated to retain a 23% capacity reserve after completing the standard 180-second mission profile (60 seconds of climb and 120 seconds of distance). However, practical flight testing of the first prototype, where a telemetry system was used, induced a revision of this energy budget. To safely accommodate three loiter turnarounds and the final landing approach, the safety factor was increased to 1.43. This adjustment provides additional 41 seconds of flight time beyond the primary 180-second mission while maintaining a 43% battery capacity reserve (storage level), essential to preserve the battery life. Consequently, the team upgraded to a Tattu® Gens Ace 3S 60C 3600 mAh LiPo battery. This power source fulfills the mandatory continuous discharge requirement of at least 40 A and delivers performance on par with the initial selection.

5.4 Motor Fine-tuning

The selected ESC provided the ability to alter the current timing and offer further performance optimization. This timing parameter significantly impacts the synchronization between the rotor angular position and the sequential activation of the stator coils. Configuration was managed through the ESC manufacturer's software (*JETI® Studio*).

It was observed through experimental evaluations that thrust oscillates with the timing advance angle, as illustrated by Figure 33. After several tests, a $6°$ timing advance was deemed optimal. This specific calibration yielded a 3.64% increase in thrust compared to the ESC's factory setting of $15°$.



(a) Timing analysis - static test. (b) Timing analysis - 15 m/s test. (c) Timing analysis - 30 m/s test.

Figure 33: Timing–Thrust analysis.

6 Electronic Components

6.1 Servos Selection

The torque required by each control surface is given by Equation 3, also known as Chuck Gadd's formula [11].

$$T = 10.197 \left(\frac{1}{2}\rho V^2\right) (c_f L_f)\, x_{cp,f} \sin\delta_f \frac{\tan\delta_f}{\tan\theta_s}\ , \tag{3}$$

where ρ is the air density, V is the maximum airspeed, c_f is the control surface mean chord, L_f is the surface control length, $x_{cp,f}$ is the distance of the hinge to the control surface center of pressure (assumed a worst-case scenario of $0.5c_f$), δ_f is the maximum surface deflection, θ_s is the maximum servo arm deflection from neutral point, and 10.197 is a factor added to convert the result in N.m to kg.cm.

The parameter values used, as well as the results obtained, are shown in Table 14.

Table 14: Torque required for different control surfaces.

Control Surface	Parameters	Value	Torque	SF = 1.5
Aileron	ρ [kg/m^3]	1.225	2.21 kg.cm	3.32 kg.cm
	V_{max} [m/s]	35		
	c_f [m]	0.09		
	L_f [m]	0.32		
	δ_f [deg]	14		
	θ_s [deg]	30		
Empennage	ρ [kg/m^3]	1.225	1.36 kg.cm	2.04 kg.cm
	V_{max} [m/s]	35		
	c_f [m]	0.132		
	L_f [m]	0.396		
	δ_f [deg]	11		
	θ_s [deg]	30		

When choosing the servomotors, we aimed for the lightest components, yet strong enough to provide the necessary torque to move heavily loaded surfaces. Thus, the KST X08H Plus were chosen. To further improve aerodynamics, Integrated Drive System (IDS) kits were used for the aileron servo installation, concealing it inside the wing structure. For the Fowler flap, the sizing was done using CFD analyses in ANSYS® Fluent [6] due to the complex nature of this mechanism. For this application, CHASERVO HV85 was selected for its higher torque and compact design.

6.2 Secondary Battery Selection

The avionics system battery was sized to withstand the servos peak current throughout the whole 180-second mission according to Equation 4.

$$C = \frac{I_{max}\Delta t}{3600} \times 1000\ \times SF\ [mAh] \tag{4}$$

where I_{max} is the maximum current withdrawn by the avionics system, Δt is the flight time, and SF is the safety factor used.

The sum of the peak current for all servos was 7.4 A. Since for this value the result given was 529 mAh, with a safety factor of 1.43, and the minimum capacity defined by the regulations was 600 mAh [1], the main consideration for the battery selection shifted to weight reduction. The team opted for a Tattu 2S 75C 750mAh battery, which was the lightest solution analyzed.

7 Circuits Assembly

To achieve a lighter and cleaner electronics integration, the team opted to assemble a custom wiring harness rather than using COTS extensions. An advantage of this approach is the reduction of intermediate connectors, which mitigates failure points.

To safely handle the combined peak current drawn by all servos, a single 20AWG master power bus (one positive and one negative cable) was implemented. From this central master set, the power is distributed to each individual connector using lighter 22AWG cables. While the servos share this common power and ground bus, each retains an independent Pulse Width Modulation (PWM) signal wire to ensure precise control. PowerBox Systems® Premium Servo wire was selected for the entire assembly due to its low mass density of 11.3 g/m. This centralized power distribution architecture significantly reduced the total mass of the avionics circuit while also being a much more organized airframe assembly.

7.1 Mass Prediction Validation

The predicted empty mass of the aircraft was 3.722 kg, while the measured value of the second prototype was 3.366 kg, as shown in Table 15. This reduction is mainly associated with structural optimization performed during the manufacturing phase, particularly in the fuselage and wing.

As detailed in Table 15, the fuselage mass was significantly lower than expected due to material reduction in low-stress regions.

In contrast, the V-tail and Fowler flap systems resulted in higher masses, mainly due to adhesive contributions not considered in the initial estimation. The landing gear mass was slightly below the predicted value, indicating a conservative initial assumption.

Overall, the mass prediction approach provided a consistent estimation of the aircraft mass, with deviations primarily linked to manufacturing and assembly effects.

Table 15: Component mass comparison.

Category	Component	Pred. [g]	Real [g]
Structures	Central panel	551	496
	Wing tips	674	610
	Fuselage	1032	753
	V-tail	60	126
	Fowler flap	150	164
	Landing gear	340	304
Propulsion & electronics	Motor	108	108
	Propeller	20	20
	ESC	109	109
	Main battery	258	245
	Secondary battery	39	39
	Receiver	16	11
	Servos	78	78
	Harness	87	87
	Measurement box	150	150
Assembly	Screws, glues, misc.	50	66
Total		**3722**	**3366**

8 Manufacturing

The following section outlines the manufacturing methodologies for each subsystem, including fabrication procedures. Composite laminates were manufactured in-house using epoxy resin, vacuum bagging, and a 24-hour curing process, while CNC-machined as well as 3D-printed components were also produced internally.

8.1 Wing and V-tail

The wing manufacturing process required the production of external molds for the composite sandwich structure. The molds for the wingtips and center panel were CNC-machined in Medium-Density Fiberboard (MDF) using the software Autodesk® Fusion 360 toolpaths [12].

After machining, the surfaces were sanded and sealed and before the lamination process, a few layers of polyvinyl alcohol (PVA) release agent were applied. Using these molds, the sandwich-structured composite was manufactured through a wet lay-up process.

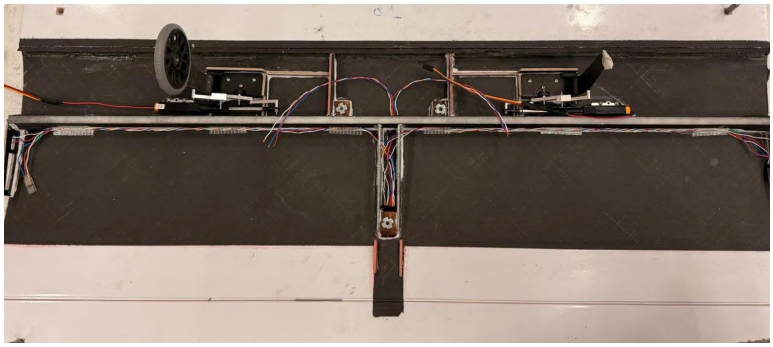
To support the internal structure, the alignment jigs were manufactured from laser-cut plywood, ensuring the correct position of the spar, ribs, landing gear and Fowler flap. The wingtip spars along with the leading edge were built with 3D-printed molds and additional internal components were CNC-machined from plywood and Airex®.

A male connector tube was used as a mold during fabrication of the connections between the wing panels to minimize clearances, and shrink tape was used to improve accuracy.

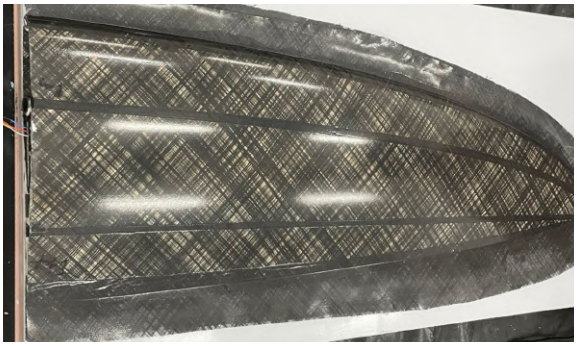


Figure 34: V-tail mold and jig.

Furthermore, the V-tail molds were manufactured following the same methodology described for the wing, however, SikaBlock® M700 was used due to material availability rather than technical considerations. Figures 34 and 35 show the manufacturing stages for the empennage, central wing panel and the wingtip.



(a) Central wing panel during manufacturing.



(b) Final manufactured wingtip.

Figure 35: Wing manufacturing stages.

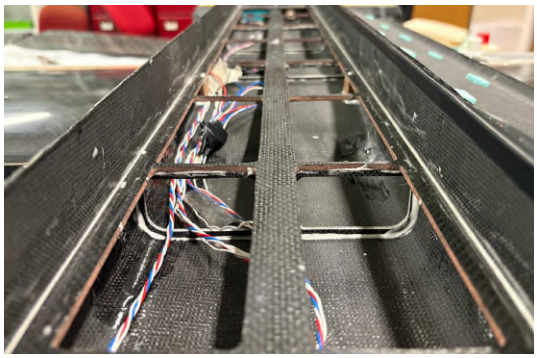
8.2 Fuselage

In contrast with Section 8.1, in which the molds were fabricated from MDF, the central and aft fuselage molds were produced using 3D printing, allowing the fabrication of complex geometries. The central fuselage mold was divided so that the lower part forms the main fuselage structure, while the upper part acts as a lid, assembled in a hinge-like manner.

The mold surfaces were initially sanded to smooth out layer lines and putty was applied at the joints between printed parts to ensure continuous leveling, following the same procedure as for the wing molds. The composite skins were then manufactured through the same process, after which Rohacell® and Airex® components, laminated with carbon fiber, were CNC-machined to produce internal frames with exact tolerances, as well as the structural tray. The aft fuselage sections were then bonded together, using carbon fiber strips in the forward region, while near the V-tail a dedicated mold was used to ensure proper fit and surface continuity. Figure 36 present the lower aft fuselage laminate as well as the final assembled fuselage internal structure.



(a) Lower aft fuselage laminate.



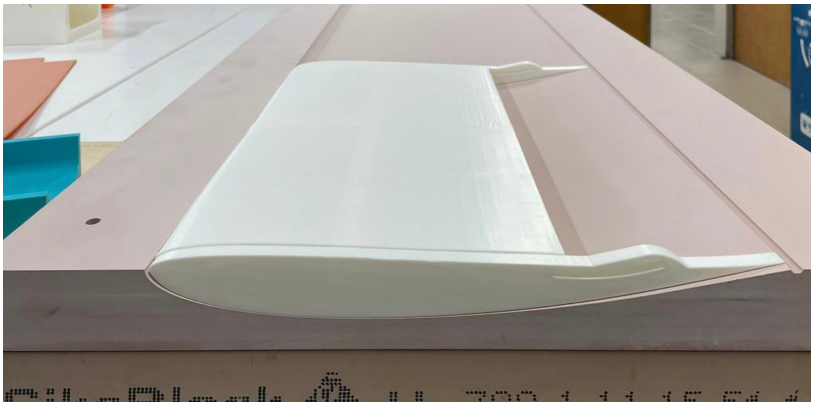
(b) Final assembled fuselage.

Figure 36: Fuselage manufacturing stages.

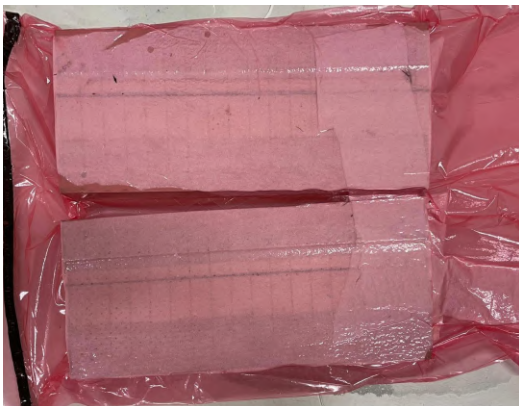
8.3 Fowler Flap

The initial concept, which consisted of an extruded polystyrene (XPS) core laminated with carbon fiber, was abandoned because the hot-wire cutting process caused distortions. As an alternative, a structural configuration composed of skin, ribs, and an internal spar was adopted.

The skin was laminated using two molds manufactured and treated the same way as the empennage, employing a sandwich configuration. The spar was manufactured using an Airex® core with carbon fiber faces, together with three ribs and a carbon fiber leading edge required to put together the skin. Again, the components were assembled using plywood assembly jigs. The lateral ribs were manufactured in carbon fiber, using both unidirectional and forged laminates, with 3D-printed molds. A prototype and the flap lamination vacuum is shown in Figure 37.



(a) First Fowler flap prototype.



(b) Fowler flap lamination vacuum.

Figure 37: Fowler flap manufacturing stages.

8.4 Landing Gear

The landing gear system was manufactured by integrating the structural tray, the main strut, the actuation links, and the wheels. In particular, the structural tray was carefully machined from aluminum to ensure the required dimensional accuracy and fit. The main strut was composed of six layers of woven carbon fiber oriented at $\pm 45^{\circ}$ and eight layers of unidirectional carbon fiber, which were sanded beforehand to ensure compliance with dimensional tolerances. In addition, the multi-link mechanism consisted of three aluminum links connected by steel pins, whereas the wheel was manufactured from PA6-CF using additive manufacturing.

9 Conclusion and Outlook

For this year's ACC edition, UBIAT faced an important transition period. This was the first year in which the team operated without the experienced members who had previously founded and consolidated the project, making this year a critical validation of the team's ability to retain knowledge, transfer technical experience to younger students, and independently execute a complete aircraft design cycle. To support this process, the team decided to develop three aircraft until the competition start, each with a specific purpose, allowing the team to gain experience, identify weaknesses, and implement corrections before the final competition aircraft. The first prototype represented a successful milestone, having flown almost twenty times and provided essential telemetry and flight-test data. These flights allowed the team to better understand the aircraft sizing model, validate assumptions, and improve the *Excel*-based sizing tool [4] and supporting design methodologies. In four months, the new team developed the sizing spreadsheet, built several auxiliary tools, sized the aircraft, and manufactured a functional prototype, which represented a significant achievement.

The second prototype was built during the detailed design phase, meaning that design refinement and manufacturing were conducted in parallel. Its construction was completed in March, and the aircraft performed nine flights. This prototype was mainly used to validate the Fowler flap and the retractable landing gear. The latter revealed several issues, including problems in the carbon support, the pins, and the connection between the wheel and the strut. The second prototype eventually crashed after one of the empennage connections failed, inducing aeroelastic effects and loads that tore the tail during flight.

Despite these difficulties, this season represented a major step forward for the team. It was the year in which the team manufactured the highest number of aircraft to date, with three aircraft built in record time, each one serving a different technical and educational purpose. The team also achieved its strongest sponsor engagement so far, which enabled the acquisition and renewal of laboratory tools and machines. In addition, several outreach and technical events were organized, including Sponsors' Day, used to present the team's work and competitions, and a Bootcamp for AeroCup, a Design/Build/Fly-style competition hosted in Portugal.

From a technical standpoint, the team aimed at improving its manufacturing processes, integrating a Fowler flap and a refined retractable landing gear, and developing a more robust and tidier avionics system. With the development of two prototypes prior to the final aircraft production, as well as the extraction and analysis of telemetry data, UBIAT managed to assess and validate the sizing stage and obtain experimental data that played a crucial part in optimizing the aircraft design. Throughout the project and construction phases, the team identified several challenges. Since this was the first implementation of IDS kit integration, wiring harness production, and Fowler flap development, the overall design process required extensive research and multiple design iterations before the final configuration was achieved. However, it was concluded that these approaches signify a lighter and more aerodynamically efficient design, further improving the aircraft capabilities. The encountered difficulties allowed the team to address real industry constraints, workflows, and develop new solutions with the intent of achieving the optimal design for this competition. With two months left for the first day of ACC2026, UBIAT will focus on mitigating failure points and optimizing both the landing gear and Fowler flap systems. These will be accompanied by rigorous tests and a final flight validation, ensuring every detail works as intended.

References

[1] Akamodell Stuttgart. *Air Cargo Challenge 2026 – Participation Handbook*, 2025. Available: https://aircargochallenge.de/ [Accessed 2026].

[2] "Python", [Online]. Available: https://www.python.org/. [Accessed 2026].

[3] "XFOIL", [Online]. Available: https://web.mit.edu/drela/Public/web/xfoil/. [Accessed 2026].

[4] Microsoft. "Office 365", [Online]. Available: https://www.microsoft.com/en-us/microsoft-365/. [Accessed 2026].

[5] "*XFLR5*", [Online]. Available: https://www.xflr5.tech/xflr5.htm. [Accessed 2026].

[6] ANSYS Inc. "Ansys® Academic Research Mechanical 2025". [Online]. Available: https://www.ansys.com/ [Accessed 2026].

[7] Dassault Systèmes®. "Solidworks". [Online]. Available: http://www.solidworks.com/ [Accessed 2026].

[8] S.W. Tsai and E.M. Wu, "A General Theory of Strength for Anisotropic Materials," *Journal of Composite Materials*, vol. 5, no. 1, pp. 58–80, 1971.

[9] R.M. Jones, *Mechanics of Composite Materials*, 2nd ed. Taylor & Francis, 1999.

[10] "AeroDesign Propeller Selector". [Online]. Available: http://www.hoppenbrouwer-home.nl/ikarus/software/propselector.htm. [Accessed 2025].

[11] Gadd, C., *Servo Sizing Formula*. Available: https://www.mnbigbirds.com/Servo%20Torque%20Caculator.htm

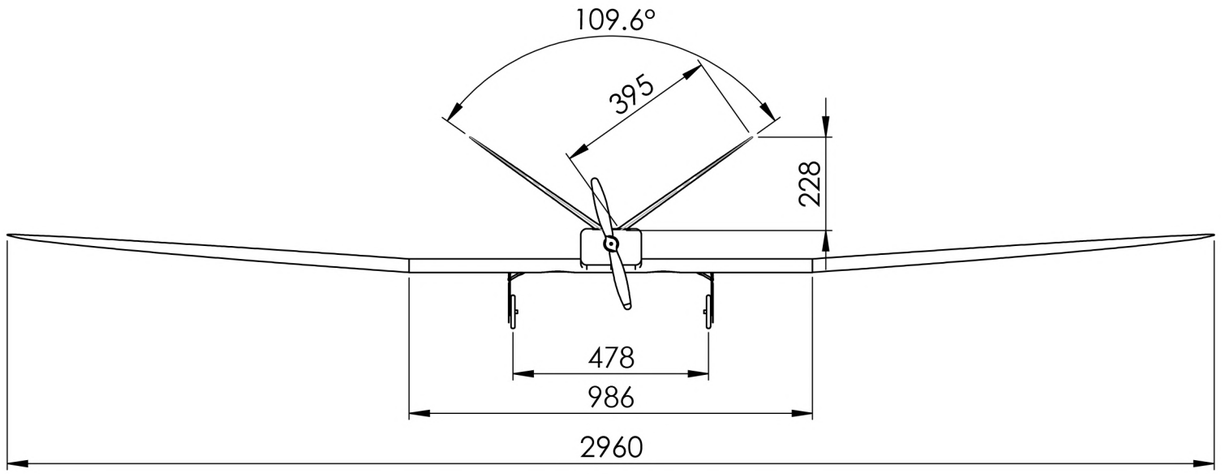
[12] Autodesk®, "Fusion 360", [Online]. Available: https://www.autodesk.com/products/fusion-360. [Accessed 2026].

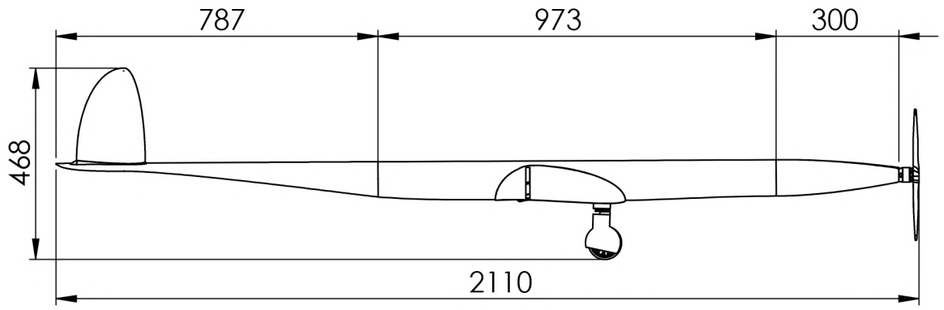
[13] Daniel P. Raymer (1992). *Aircraft Design: A Conceptual Approach*, American Institute of Aeronautics and Astronautics, 2nd edition.

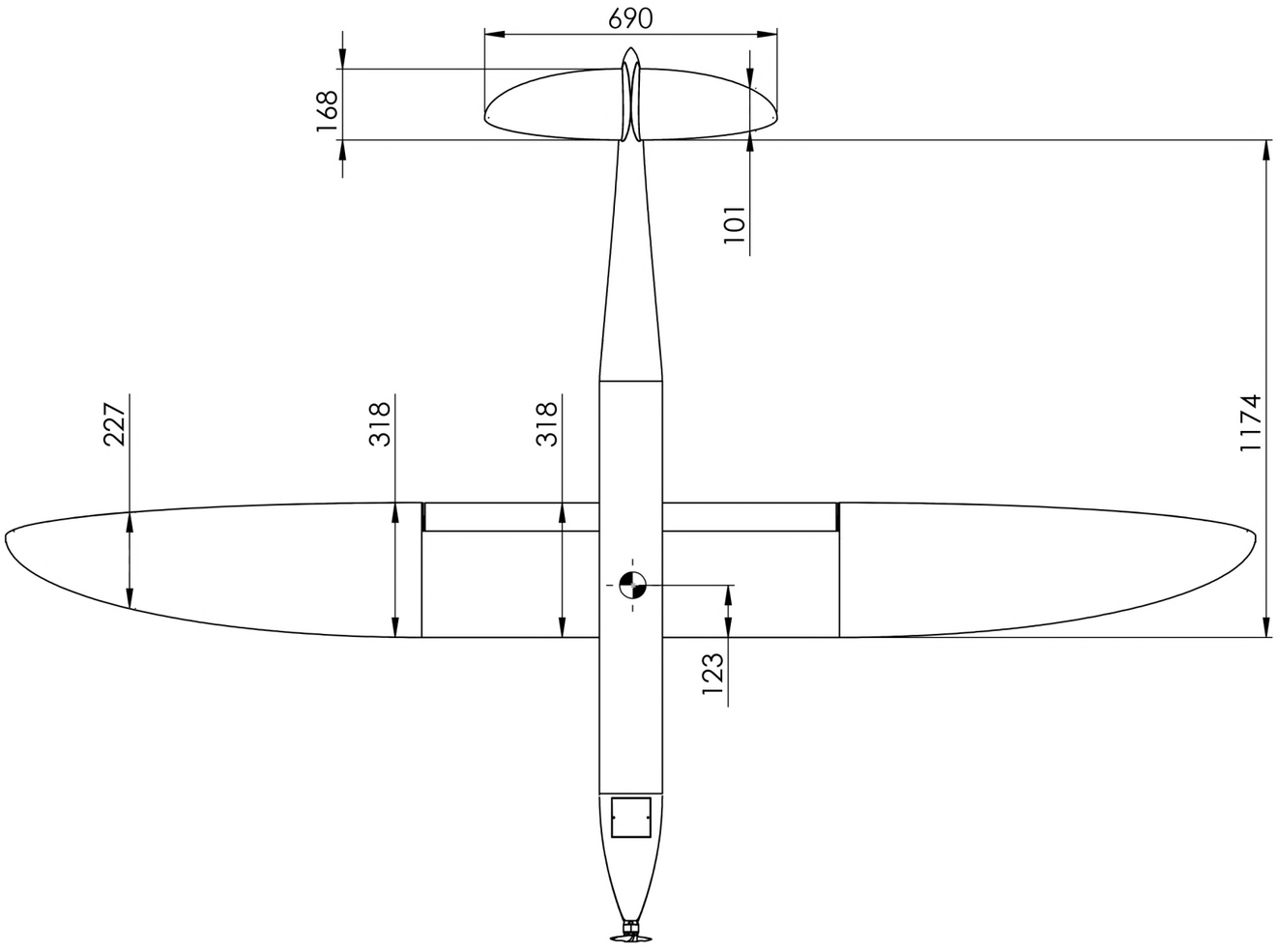
[14] Luiz Eduardo Miranda José Rodrigues (2014). *Fundamentos da Engenharia Aeronáutica com aplicações ao projeto SAE-AERODESIGN: Aerodinâmica e Desempenho*, Salto, 1st edition.

[15] ASTM International, "ASTM D3039/D3039M – Standard Test Method for Tensile Properties of Polymer Matrix Composite Materials," ASTM International, West Conshohocken, PA.

[16] ASTM International, "ASTM D3518/D3518M – Standard Test Method for In-Plane Shear Response of Polymer Matrix Composite Materials by Tensile Test of a $\pm 45°$ Laminate," ASTM International, West Conshohocken, PA.







	Wing	V - Tail
Airfoil	"Super"	NACA 0008
Area	0.794 m²	0.100 m²
Volume Coefficient	---	V_H=0.439 V_V = 0.016
Aspect ratio	10.74	6
Dihedral angle	4°	35.2°
Angle of attack	-0.6°	-1.15°
Maximum payload		16 cans
Announced payload		12 cans

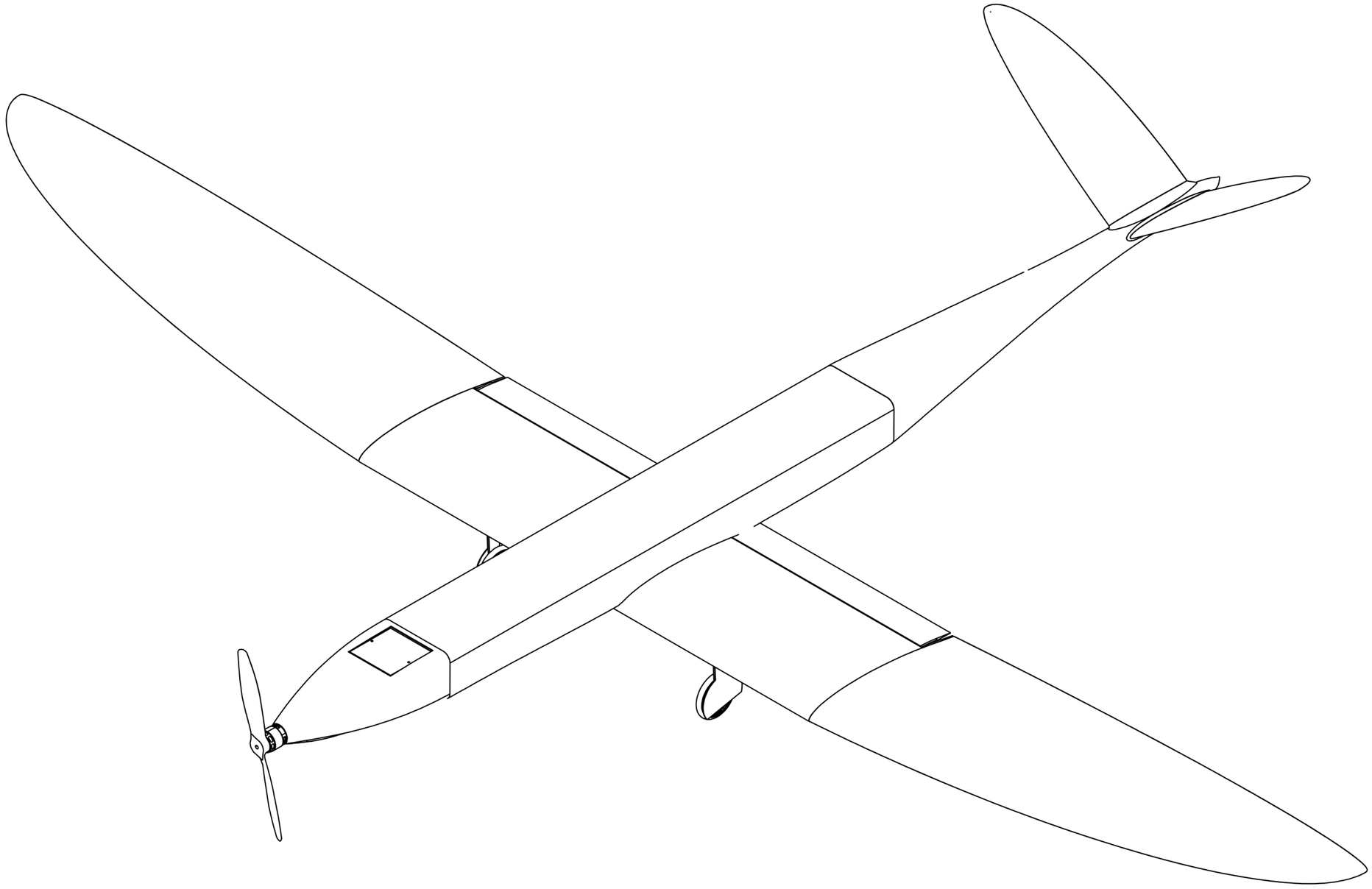
Air Cargo Challenge 2026

UBI Aeronautics Team, Team No. 13

UBIAT
UBI AERONAUTICS TEAM

All lengths in millimeters	1/4
All angles in degrees	Scale 1:15
30/04/2026	
"Bock"	A3

3-view drawing



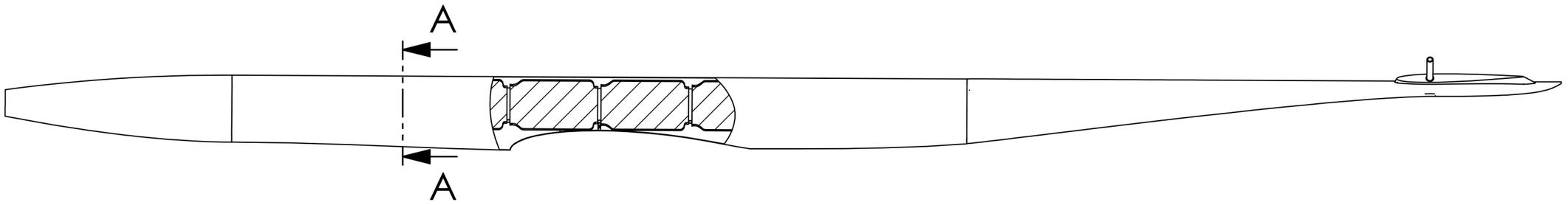
Air Cargo Challenge 2026

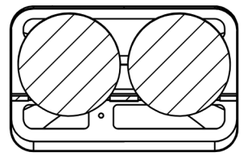
UBI Aeronautics Team, Team No. 13

UBIAT
UBI AERONAUTICS TEAM

All lengths in millimeters	2/4
All angles in degrees	Scale 1:7
30/04/2026	
"Bock"	A3

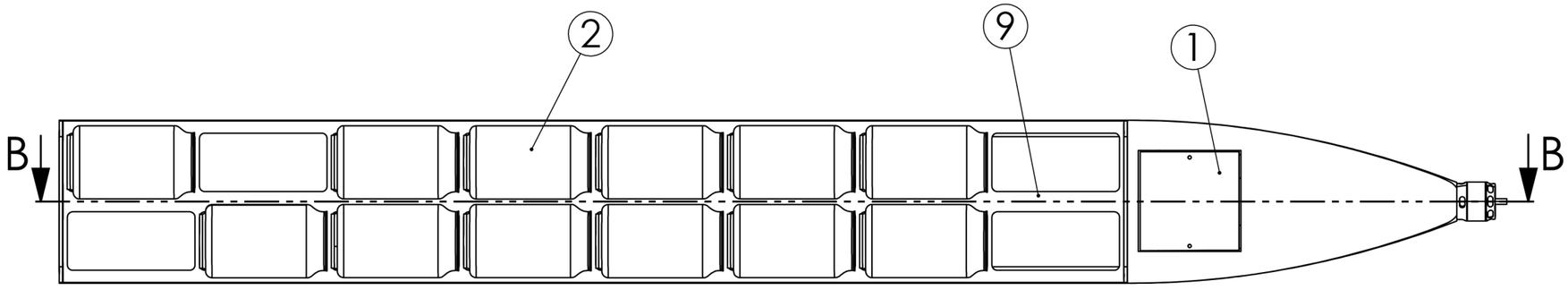
Isometric drawing





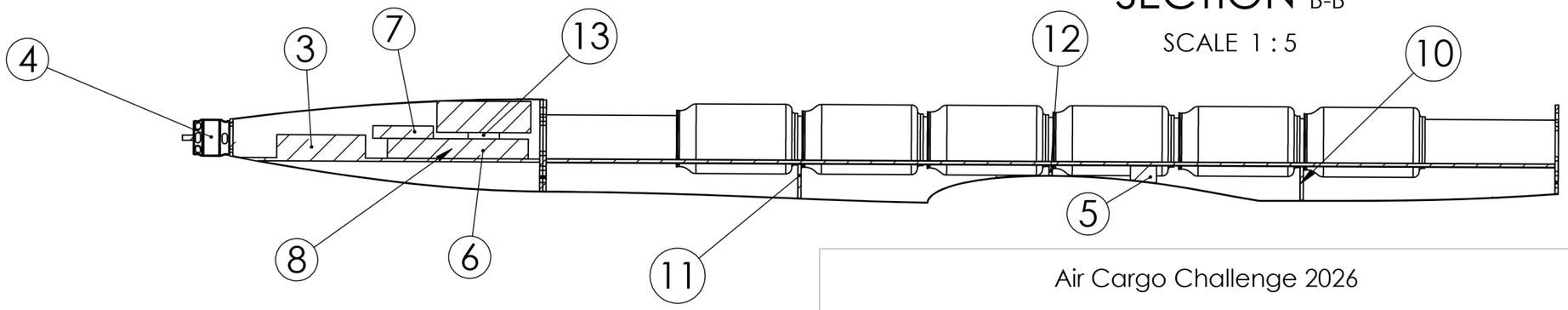
SECTION A-A

SCALE 1 : 4



SECTION B-B

SCALE 1 : 5



1	Measuring box
2	12 cans layout
3	ESC
4	Electric motor
5	Wing attachment block
6	Main battery
7	2nd battery
8	RC receiver
9	Structural tray
10	Structural frame 1
11	Structural frame 2
12	Strucutral frame 3
13	Measuring box mount

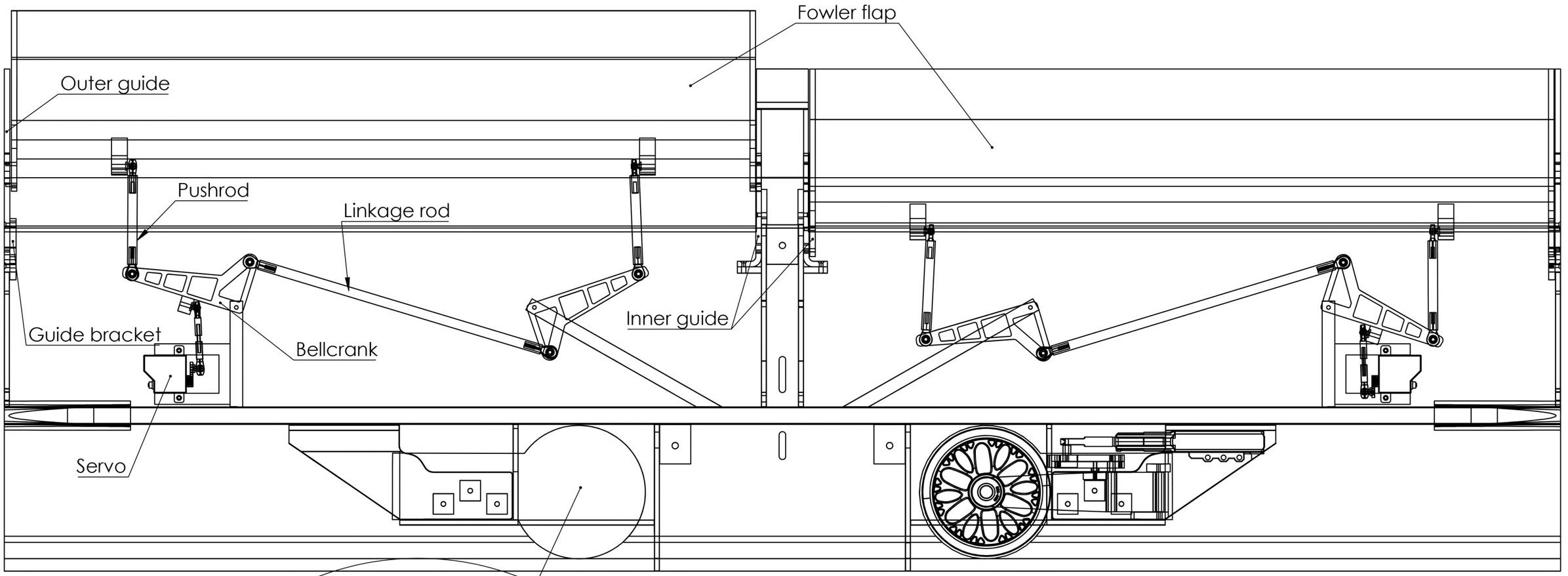
Air Cargo Challenge 2026

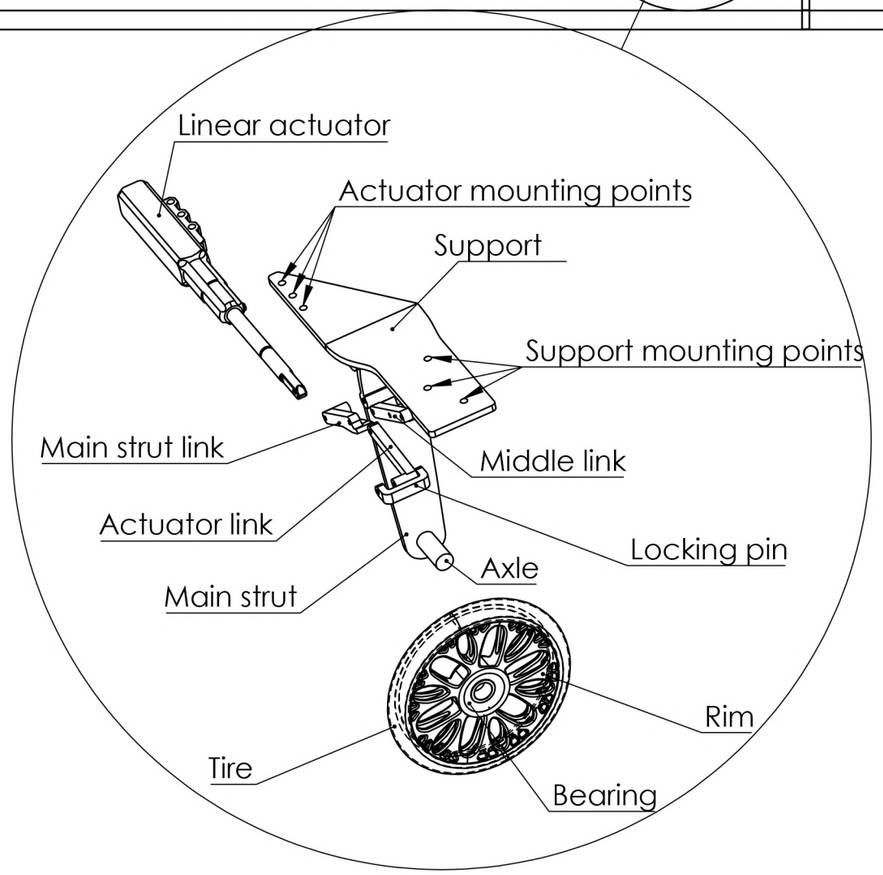
UBI Aeronautics Team, Team No. 13

UBIAT
UBI AERONAUTICS TEAM

All lengths in millimeters	3/4
All angles in degrees	Scale 1:6
30/04/2026	
"Bock"	A3

Cargo bay, RC receiver position, position of measuring equipment





Air Cargo Challenge 2026

UBI Aeronautics Team, Team No. 13

UBIAT
UBI AERONAUTICS TEAM

All lengths in millimeters	4/4
All angles in degrees	Scale 1:2.5
30/04/2026	
"Bock"	A3

Retractable Landing Gear and Fowler Flap assembly